

## Testing the solar activity paradigm in the context of exoplanet transits

CAROLUS J. SCHRIJVER<sup>1</sup>

<sup>1</sup>*Johannes Geiss Fellow at the International Space Science Institute,  
Hallerstrasse 6, 3012 Bern, Switzerland*

(Received 2019 October 24; Revised 2019 December 21; Accepted 2020 January 3)

Accepted for publication in ApJ

### ABSTRACT

Transits of exoplanets across cool stars contain blended information about structures on the stellar surface and about the planetary body and atmosphere. To advance understanding of how this information is entangled, a surface-flux transport code, based on observed properties of the Sun's magnetic field, is used to simulate the appearance of hypothetical stellar photospheres from the visible near 4000 Å to the near-IR at 1.6 μm, by mapping intensities characteristic of faculae and spots onto stellar disks. Stellar appearances are computed for a Sun-like star of solar activity up to a star with mean magnetic flux density  $\sim 30\times$  higher. Simulated transit signals for a Jupiter-class planet are compared with observations. This (1) indicates that the solar paradigm is consistent with transit observations for stars throughout the activity range explored, provided that infrequent large active regions with fluxes up to  $\sim 3 \times 10^{23}$  Mx are included in the emergence spectrum, (2) quantitatively confirms that for such a model, faculae brighten relatively inactive stars while starspots dim more-active stars, and suggests (3) that large starspots inferred from transits of active stars are consistent with clusters of more compact spots seen in the model runs, (4) that wavelength-dependent transit-depth effects caused by stellar magnetic activity for the range of activity and the planetary diameter studied here can introduce apparent changes in the inferred exoplanetary radii across wavelengths from a few hundred to a few thousand kilometers, increasing with activity, and (5) that activity-modulated distortions of broadband stellar radiance across the visible to near-IR spectrum can reach several percent.

*Keywords:* Solar activity — Solar spectral irradiance — Stellar photospheres — Stellar activity — Exoplanet astronomy — Transit photometry

### 1. INTRODUCTION

Magnetic activity of cool stars, as in the case of the Sun, manifests itself in a photosphere in the form of a mixture of bright faculae and dark pores and spots. Their distribution and number is modulated by the stellar dynamo, which in the case of the Sun is reflected in the sunspot cycle. Knowledge of the locations and sizes of active regions and their spots on stars other than the Sun is limited by the means available to study them,

generally through the modeling of photometric modulation or of (Zeeman) Doppler signals associated with stellar rotation. These methods generally have to assume that the structures on the stellar surfaces do not evolve on the time scale of a rotation; that clearly is not the case for individual active regions on a star with a rotation rate like that of the Sun, nor is it likely to hold on faster rotators where the rate of flux emergence is significantly elevated. Doppler signals in principle carry information on the latitude of the source regions, but this is only recoverable if the Doppler signal of rotation is comparable to, or exceeds, that of the thermal and convective velocities; for a star like the Sun, with a photospheric thermal line width equivalent to some

karelschrijver@gmail.com

Corresponding author: C.J. Schrijver

7 km/s, the maximum rotational Doppler signal exceeds the thermal width only for stars with rotation periods below  $\approx 7$  days. For stars with a rotation axis near the plane of the sky, both hemispheres are accessible to these methods, but none can disambiguate on which hemisphere the features reside that lead to the observed signals. Magnetic field maps are even harder to reconstruct than spot maps; for a discussion of methods and results, see the review by [Reiners \(2012\)](#).

Because of these intrinsic challenges, only large-scale, slowly evolving structures can in principle be recovered with some reliability, as significant simplifications are made by the models and regularization algorithms applied to limit degeneracies of possible but not necessarily plausible solutions. Thus, angular resolution is limited to large patches commonly spanning tens of astrometric degrees; for example, [Lanza \*et al.\* \(2007\)](#) find that the longitudinal resolution achievable through spot modeling of rotational modulation of a star of solar activity is typically some  $60^\circ$ , while [Strassmeier \(2009\)](#) notes that the smallest “spots” found under optimal conditions for Doppler imaging are some  $10^\circ \times 10^\circ$ , the latter just reaching the size of the largest (rare) sunspots. For slow rotators, with  $v \sin(i) \leq 5$  km/s which are the focus of the present study, however, the resolution achievable by Zeeman-Doppler imaging is limited to some  $30^\circ$  while much of the flux in a map is lost as signals with opposite polarizations largely cancel ([Lehmann \*et al.\* 2019](#)).

Despite the limitations of how stellar magnetic activity can be studied, much has been learned about activity patterns (such as the apparent existence of persistently active longitudes) and stellar differential rotation (albeit commonly with ambiguity of sign). But the emergence patterns as a function of time and latitude, the size distribution of active regions, the magnitude of convective flux dispersal, the strength and profile of meridional advection, and properties of the full spectrum of starspots remain largely beyond our observational grasp. For reviews on stellar dynamos, starspots, and stellar magnetic fields, see, for example, [Berdyugina \(2005\)](#), [Brun and Browning \(2017\)](#), [Reiners \(2012\)](#), and [Strassmeier \(2009\)](#).

The discovery of transiting exoplanets has opened up a novel way of studying stellar surface structures: the transiting exoplanet acts as an occulting disk moving across the features within the transit path. The spatial resolution that can be attained by this method is in principle limited only by the size of the occulting disk and its movement across the stellar disk within the time required for an exposure with sufficient signal-to-noise ratio (S/N). If the transit is sufficiently fast, the background photospheric features can be assumed constant,

so that difference spectra (or passband intensity differences) can be computed between the unocculted and occulted signals to acquire a pure spectrum of what resides behind the exoplanetary disk (see [Dravins \*et al.\* 2017](#), for an example of studying stellar granulation). For slower transits, or to obtain higher resolution, the time series of the transit can be studied as a convolution problem. Light-curve analyses suggest spot sizes down to  $\sim 3^\circ$  in diameter (*e.g.*, [Silva-Valio and Lanza 2011](#); [Valio \*et al.\* 2017](#)).

This fairly novel way to achieve high-resolution information for stellar surface structures along the transit path is of critical importance to studying exoplanetary atmospheres through transit spectroscopy (*e.g.*, [Seager and Sasselov 2000](#); [Brown 2001](#)): the light passing through the exoplanetary atmosphere contains information about the atmospheric structure, but to extract it unambiguously, the properties of the light source need to be known. That light source is the photospheric patch that lies behind the exoplanetary atmosphere in the line of sight towards the observer, as discussed in detail by, *e.g.*, [Rackham \*et al.\* \(2018, 2019b\)](#), although some scattering in the atmosphere of the exoplanet needs to be allowed for. This presents a challenge and opportunity combined: the emission properties of the stellar surface structures along the transit trajectory as well as the transmission properties of the exoplanetary atmosphere need to be analyzed in a joint study of the spectrum that carries information on both source and absorber (*e.g.*, [Kowalski \*et al.\* 2019](#); [Rackham \*et al.\* 2019a](#)).

The stellar magnetic activity can affect observed spectra whose interpretation can lead to ambiguities between stellar surface (and, of course, chromospheric) features and the chemical composition, clouds, and particulate hazes in an exoplanetary atmosphere, arising in the interpretation of broadband measurements or high-resolution line spectroscopy (see, for example, [Cauley \*et al.\* 2018](#); [Pinhas \*et al.\* 2018](#)).

Until recently, transit spectroscopy studies often assumed that the transit light source is the same as the spectrum of the average unocculted disk. More recently, detailed shapes of limb darkening (*e.g.*, [Espinoza and Jordán 2015](#)) and modeling of spots along the transit path have come into play, with an occasional study also allowing for bright facular regions (*e.g.*, [Oshagh \*et al.\* 2014](#); [Murgas \*et al.\* 2019](#); [Bruno \*et al.\* 2020](#), and others, see below), albeit characterized by a simple brightness contrast or single temperature without accounting for limbbrightening effects. Transit light-curve analyses in the literature go about inferring properties of stellar surface structures from observations, generally assuming simplified features on the stellar surface: often simply

circular starspots, with or without a variety of brightnesses (or assumed spot temperatures), some with associated facular regions (which may all be assumed to be identical except for sizes, or may allow for some simple ad hoc spectral effects), either surrounding these spots or allowing patches elsewhere on the stellar surface. Understandably, the number of free parameters is kept low because present-day observations can offer only a limited number of constraints.

The purpose of this paper, in contrast, is to use forward modeling of patterns of stellar magnetic fields and their photospheric effects based on observed characteristics of the Sun’s magnetic field. Here, too, even if limiting this study to stars like our G2V Sun, there is an assumption, and indeed one that has many facets, namely that the solar paradigm applies to other stars, and specifically to stars of substantially higher magnetic activity than exhibited by the Sun. This study is thus meant as an exploration through attempted falsification of the validity of the solar example. At the same time, it provides quantitative insight into the impacts of stellar activity on information about exoplanetary atmospheres extracted from transit spectroscopy. Among the multitude of choices for such a study, I choose to use the full richness of surface field patterns and model-derived limb-brightening curves for faculae in areas of different mean magnetic flux density, while stopping short of full spectral synthesis. For approaches in which the full observed spectrum is analyzed or a model spectrum computed but with highly simplified assumptions about stellar surface features, see, for example (ordered in time, generally following a path toward increasing complexity) Pont *et al.* (2008); Sing *et al.* (2011); Herrero *et al.* (2016); Rackham *et al.* (2018, 2019b).

The hypothesis that the solar paradigm and the derived surface flux-transport model hold for stars of different activities has been extensively tested (*e.g.*, Schrijver and Zwaan 2000). The model applied here was used to understand how solar and cool-star radiative losses from chromospheres and coronae are related (Schrijver 2001), supporting the applicability of the solar paradigm for stellar studies. For the most active stars, the phenomena of extremely large and high-latitude starspots present challenges to the solar paradigm (but see Schrijver and Title 2001), and for this reason the present study stops at stars of moderate activity. Among the issues that will come up is the phenomenon of the starspot: light curves of active stars often suggest starspots much larger than sunspots. However, the low resolution that can be achieved when mapping stellar surface features leaves open the possibility that such large stellar spots are in fact clusters of smaller, more solar-like ones, which

at least for moderately active stars appears to be compatible with stellar data (*e.g.*, Solanki and Unruh 2004), and also with lifetime estimates of starspots assuming these are dispersed subject to surface convective flows (Bradshaw and Hartigan 2014).

In this paper, I experiment with a flux-transport model developed for the Sun, discussed in Sect. 3.1. Model stellar radiances are computed using a three-component approach that includes a quiet background photosphere, a component associated with magnetic field in magnetic plages and network (referred to here collectively as faculae), and spots (including their smaller counterparts, the pores). Modeling of the solar irradiance has shown such an approach to be successful, see, *e.g.*, Fligge *et al.* (1998); Yeo *et al.* (2017). Properties of solar faculae, pores, and spots, and a quiet-Sun limb-darkening curve are then used to render the appearance of Sun-like stars of different activity at two different wavelengths in the visible and one in the near-IR. Subsequently, virtual exoplanet transits are performed to compute the color-dependent transit curves and residuals (Sect. 3.3). Simulated rotational modulation signals (Sect. 4) and transit residuals (Sect. 5) are then discussed and compared to examples of observed signals in a few cool dwarfs (presented in Sect. 2), before I conclude the paper with discussion and conclusions (Sects. 6 and 7).

## 2. A SELECTION OF COOL STARS TRANSITED BY LARGE EXOPLANETS

The model discussed in Sect. 3 relies on observed properties of the Sun’s surface activity, including the shape of the sunspot cycle, the frequency distribution of active-region sizes, their distribution to form the butterfly diagram, their typical tilt angles relative to the equator, their nesting property for successive generations of emergence, the (super-)granular random-walk dispersal, and the large-scale meridional advection and differential displacement. None of these properties are known well enough for other types of stars (be it from observations or through modeling), so that application of the model to anything but an early G-type dwarf star is not warranted without determination of changes in the above properties with spectral type. Similarly, for the generation of transit light curves, note that the wavelength and position-dependent properties of sunspots and faculae are known for the Sun, but are insufficiently clear for other types of stars. In view of all that, the model is applied here only for a Sun-like star, and consequently the comparison to observations is limited to G- and early K-type main-sequence stars.

**Table 1.** Selection of active G- and early-K type dwarf stars transited by Jupiter-sized exoplanets. Listed are: name, spectral type, rotation period, exoplanetary radius  $R_p$  relative to the stellar radius  $R_*$ , the estimated relative impact parameter for the transit  $d_t$ , and characteristic peak-to-trough amplitude of the rotational modulation of the stellar brightness. The next-to-last column shows whether evidence is seen in the transit residuals for surface inhomogeneities (with estimated maximum magnitude if seen, or the detection threshold if not).

Star	Spectral type	$P_{\text{rot}}$ (days)	$R_p/R_*$	$d_t^d$	Rotation modul.	Transit features?	Reference(s)
V1298 Tau	K0–K1.5	2.87	0.071	0.24	$\approx 3\%$	Y( $\sim 0.15\%$ )	David <i>et al.</i> (2019)
CoRoT-2	G7 V	4.5	0.172	0.25	$\approx 3 - 4\%$	Y( $\sim 0.6\%$ )	Silva-Valio and Lanza (2011)
POTS-1	K5 V	$\gtrsim 7^a$	0.164	0.45	?	N( $\lesssim 0.7\%$ )	Koppenhoefer <i>et al.</i> (2013)
HAT-P-23	$\approx G1$	$\approx 7^b$	0.13	0.33	?	N( $\lesssim 0.2\%$ )	Bakos <i>et al.</i> (2011)
WASP-170	G1 V	7.8	0.118	0.67	$\approx 2\%$	Y( $\sim 0.3\%$ )	Barkaoui <i>et al.</i> (2019)
CoRoT-9	G3 V	$8^b$	0.115	0.16	?	Y( $\sim 0.2\%$ )	Lecavelier des Etangs <i>et al.</i> (2017)
WASP-36	G2 V	$\approx 11^c$	0.138	0.66	?	N( $\lesssim 0.05\%$ )	Mancini <i>et al.</i> (2016)
Kepler-17	G2 V	12	0.138	0.26	$\approx 1 - 3\%$	Y( $\sim 0.3\%$ )	Valio <i>et al.</i> (2017), Lanza <i>et al.</i> (2019)
HD 189733	K1–K2 V	12	0.144	0.65	$\approx 1.5\%$	Y( $\sim 0.3\%$ )	Sing <i>et al.</i> (2011)
WASP-52	K2 V	16–18	0.167	0.74	$\approx 1\%$	Y( $\sim 0.3\%$ )	Hébrard <i>et al.</i> (2013), Bruno <i>et al.</i> (2020)
Kepler-71	G7–G9 V	20	0.136	–	$\approx 1\%$	Y( $\sim 0.3\%$ )	Zaleski <i>et al.</i> (2019)
WASP-6	G8 V	24	0.141	0.28	$\approx 1\%$	Y( $\sim 0.3\%$ )	Tregloan-Reed <i>et al.</i> (2015), Nikolov <i>et al.</i> (2015)

<sup>a</sup> Based on  $v \sin i \leq 5.3$  km/s, and an estimated radius of  $0.7R_\odot$ ; <sup>b</sup> based on  $v \sin i = 5.4$  km/s in the SIMBAD database; <sup>c</sup> based on  $v \sin i = 4$  km/s in the SIMBAD database; <sup>d</sup> estimated from orbital inclination, orbital semi-major axis, and stellar radius as listed in the tables at [exoplanet.eu](http://exoplanet.eu).

Table 1 lists a selection of relatively active G- and early K-type cool dwarf or subgiant stars that are transited by giant exoplanets for which transit light curves and transit residuals have been analyzed in the literature. The table lists a few of the stellar properties, followed by characteristic peak-to-trough values of the relative rotational modulation; the latter are rough estimates based on observed light curves, averaging over a series of about a dozen rotations. There are also notes on whether there are significant signatures of stellar surface features seen in the transit residuals, and their peak relative strength. A few comments on three of these (with source references as in the table, unless otherwise given):

- CoRoT-2 is a rather young and rapidly spinning star. Photometry of 77 transits over  $\approx 30$  full stellar rotations suggested typically five dark patches interpreted as spots per transit. The patch sizes measure typically 0.25–0.8 planetary radii ( $R_p$ ), averaging at  $\approx 0.45R_p$ ,  $0.077R_*$ , or  $\approx 50,000$  km. The relative spot intensities exhibit a wide range, almost uniformly covering values from close to zero up to around 0.8, falling rapidly in frequency above that. Figure 4 by Silva-Valio and Lanza (2011) suggests a pronounced tendency for the smaller spots to be darker. As discussed in Sect. 5, this

could indicate that the larger spots are in reality clusters of dark structures with an area filling factor decreasing with increasing feature size (this relationship is not explicitly shown, but the figures suggest the scaling may be roughly linear). Rotational modulation reaches peak-to-trough values of 3%–4%, (Lanza *et al.* 2009).

- Kepler-17 is a Sun-like star, albeit more active at  $P_{\text{rot}} \approx 12$  days. Transit light-curve analyses over a period of some 1200 days, with residuals reaching  $\approx 0.4\%$ , resulted in the determination of spot properties under the transit chord. Typical spot radii range from 0.2 to  $0.7R_p$ , with a few larger ones; intensities range from about 0.2 to 0.85, with an average value of 0.55. As in CoRoT-2, there is a trend for larger spots to be brighter.
- Kepler-71 is a late-G main-sequence star with  $P_{\text{rot}} = 20$  days. Its transit residuals have been modeled in terms of both dark spots and bright faculae. The modeling suggests spot intensities widely ranging between about 0.1 and 0.9 times the unperturbed photosphere, while facular areas have relative intensities most commonly between 1.1 and 1.25 in the *Kepler* passband. The spots are

typically found to have a scale of half the exoplanet radius, while the facular regions range from about that size up to about  $1.3R_p$ , covering roughly 50–100% more area in total than the spots do.

### 3. MODEL DESCRIPTION

#### 3.1. Flux-transport model

The flux-transport model used here was developed by Schrijver (2001), with cycle modulation introduced by Schrijver and Title (2001) and with flux-decay properties as discussed by Schrijver *et al.* (2002). This same flux-transport code continues to be used in an assimilation mode for SOHO/MDI and SDO/HMI magnetogram data starting in mid-1996, see, for example, Schrijver and DeRosa (2003), and Schrijver and Liu (2008).<sup>12</sup>

Visualizations of the global field patterns are discussed below, but other realizations associated with two of the model runs here (identified as  $\mathcal{M}(\mathcal{A} = 1)$  and  $\mathcal{M}(\mathcal{A} = 30)$ ; see below in this section for their properties) can be found in Schrijver *et al.* (2003).

At each time step, a set of bipolar regions is randomly selected from a parent-distribution power-law frequency spectrum that is based on the work by Harvey and Zwaan (1993): they used magnetogram sequences throughout solar Cycle 21 (1975–1986) to determine times of maximum development of bipolar regions and with that determined the behavior of the flux-input spectrum with cycle phase. Their findings support a power-law distribution of bipolar-region sizes for which the power-law index is essentially unchanged through the cycle, so that only a multiplier is needed to describe the evolution through the activity cycle. The same spectrum is used throughout the simulated activity cycles, but modulated in time with a profile resembling a solar sunspot cycle, with successive cycles somewhat overlapping in early and late cycle phases. Stars of different activity levels are simulated by a multiplier on the cycle amplitude. As discussed below, a maximum flux for active regions is set as desired, below which the distribution is maintained the same in shape, except for an overall multiplicative factor.

These regions are then randomly distributed over a range of latitudes and with a range of tilt angles. The latitudes and tilt angles have a spread that decreases with increasing size of the region, while the mean latitude shifts from mid-latitudes toward the equator as a cycle progresses, with a 3yr phase of overlap between successive cycles, all based on the average values and scatter about those derived from solar observations. Random values are generated, drawn from parent distribution functions that are based on observed properties of solar bipolar regions, ranging from small ephemeral regions to large active regions.

The longitude of flux emergence for each bipole is in principle randomly drawn from a uniform distribution. However, this is modulated by where previously emerged regions continue to exist: on the Sun, bipolar regions have a strong tendency to emerge at locations where a previous generation emerged and often still exists. This nesting property is so pronounced that almost one in two active regions emerges inside another (Brouwer and Zwaan 1990; Harvey and Zwaan 1993). The nesting as seen for solar regions is modeled as described by Schrijver (2001). In short, the probability of emergence per unit area inside a magnetic plage region is set to 22 times that outside of a plage region (following Harvey and Zwaan 1993). Other than this hysteresis in flux emergence, no preferred longitudes are introduced.

The selected fluxes are distributed as flux concentrations over two adjacent patches of opposite polarity. Work by Schrijver and Harvey (1994) revealed that mature active regions have a mean flux density of 100–150 G (excluding spots and pores), regardless of the region’s age or size. Here, a mean flux density is chosen of 180 G (as in the original model by Schrijver (2001)) to accommodate a characteristic fraction of the flux contained in spots and pores. The regions are gradually introduced, with an equivalent rate of flux emergence of  $5 \times 10^{21}$  Mx/day (based on data from Harvey and Zwaan 1993).

The flux-transport model uses a point-source approximation for the magnetic field. These sources can be thought of as moving along a pattern of vertices that are defined by the evolving supergranular network. The properties of that cellular pattern and the characteristic displacement velocity along its vertices determine the typical mean-free path for the flux concentrations. At each time step, the flux-transport model assumes that all flux within an area with a radius equal to the typical mean-free path length for the quiet-Sun network coagulate into a single concentration prior to the next time step. This concept was successfully tested for a range of solar activity levels. The derivation of the coagula-

<sup>1</sup> Assimilation results can be viewed at <http://www.lmsal.com/forecast/>.

<sup>2</sup> Results from another flux-transport model are shown by Gibb *et al.* (2016) and Lehmann *et al.* (2019), in which also experiments with different differential-rotation and meridional-advection profiles are discussed. The main differences with the model used here are that their model describes the magnetic field as a continuous medium, does not reach down to the smallest bipoles, imposes a flux-independent diffusion coefficient, and has a distinct flux insertion algorithm that moreover does not incorporate active-region nesting.

tion radius  $r_c = 4200$  km is described in § 4 of Schrijver (2001), based on the model by Schrijver *et al.* (1997).

In reality, the supergranular and larger-scale flows that transport magnetic flux are, of course, not strictly confined to the lanes between supergranules, while moreover the supergranular cell pattern itself is evolving. Hence, the flux concentrations in the model are abstractions of patches within the photospheric field for which the diffusion approximation can be applied on scales beyond the coagulation radius. On scales below  $r_c$ , granular convective motions interact with the magnetic flux through the laws of radiative magnetoconvection, reaching a quasi-equilibrium on a time scale of a few granular turnover time scales, well below the step time of 0.25 day used in the model. Note that the diameter of the coagulation patch of  $2r_c = 8400$  km is comparable to the box width of 9000 km used for the numerical models by Norris *et al.* (2017), which is used in Sect. 3.3 to model the photospheric brightness. Hence, Sect. 3.3 uses the fluxes  $\Phi_i$  in the point sources of the surface flux-dispersal model, converted into a mean flux density of  $\Phi_i/(\pi r_c^2)$ .

The flux concentrations initiate a grid-free random walk in which step lengths are a function of the absolute flux of the concentrations, again following observed trends that show larger concentrations to be less mobile, *i.e.*, apparently more able to resist convective displacement.

These concentrations can collide to merge or (partially) cancel, and they can fragment, with collision cross sections and fractionation probabilities depending on the flux contained, as derived from solar observations.

Then, before starting on the next step, all concentrations are moved subject to the large-scale differential-rotation and meridional-flow profiles, after which a new set of bipolar regions is selected to match the average flux-input rate, which itself is modulated following the progression of an activity cycle shaped as the average sunspot cycle.

I use the following parameter settings (for details see Schrijver and Title 2001): A time step of 6 hr, a flux-dispersal coefficient of  $D = 300$  km/s<sup>2</sup> with a flux-dependent step size as described by Eqs. (A4) and (A5) in Schrijver (2001). The differential-rotation rate is set to that from Komm *et al.* (1993) and the meridional flow, tapered at high latitudes, like that of Van Ballegoijen *et al.* (1998), both as applied in the study by Schrijver and Title (2001). The half-life time scale on which flux concentrations 'decay' (*i.e.*, are randomly removed from the simulation) as introduced and described by Schrijver *et al.* (2002) is set to 5 yr. The model is set to use a fixed-amplitude cycle with equal strengths at each sunspot maximum, set to reach its peak 4 yr after

sunspot minimum, with a cycle-to-cycle overlap period of 3 yr (see Schrijver *et al.* 2002). The duration of the full magnetic cycle is set to 21.9 yr, and its associated flux-injection profile in time and latitude is as in Eq. (2) in Schrijver and Title (2001).

### 3.2. Model runs

The model is run for five different sets of only two free parameters. The first,  $\mathcal{A}$ , quantifies the amplitude of the stellar cycle; it is simply a multiplier on the frequency at which bipolar regions are inserted compared to a typical solar cycle, so that  $\mathcal{A} = 1$  is used for a run to mimic the Sun (calibrated to Cycle 21), while  $\mathcal{A} > 1$  signifies a more-active star with a more pronounced cycle. The second parameter,  $\Phi_{\max}$ , is a threshold flux in bipolar regions at which the power-law frequency spectrum of fluxes is truncated, as discussed below. The parameters and results of the five runs are summarized in Table 2.

A star like the present-day Sun is simulated as in the model developed by Schrijver (2001), here referred to as  $\mathcal{M}(\mathcal{A} = 1)$ . For this baseline solar model, the bipole-emergence rate is calibrated to the solar cycle, *i.e.* with a cycle-strength multiplier as in Schrijver and Title (2001) of  $\mathcal{A} = 1$ .

For stars like Kepler-17 and WASP-36, of solar spectral type but with rotation periods around 12 days, a coronal soft X-ray flux density is expected that is about 10 times higher than that of the Sun (*e.g.*, Patten and Simon 1996; Mittag *et al.* 2018). As the soft X-ray flux density scales roughly linearly with the surface magnetic flux density (*e.g.*, Schrijver and Title 2005) the mean surface magnetic flux density,  $\langle |fB| \rangle$  (for filling factor  $f$  and intrinsic photospheric field strength  $B$ ), should be roughly an order of magnitude higher than for run  $\mathcal{M}(\mathcal{A} = 1)$ , here particularly for the facular fields because spot fields appear to contribute little to the coronal brightness, so roughly  $\sim 150$  G. Reaching such levels of surface magnetic activity requires significant enhancements in the active-region injection frequency or mean active-region size, or both.

This estimate of the average surface magnetic flux density  $\langle |fB| \rangle \sim 150$  G for stars of about half the solar rotation period is subject to a considerable uncertainty range. One discussion of this (with associated references) can be found in Vidotto *et al.* (2014): using the five power-law scalings from various sources in the literature that are listed in their Table 3 based on Zeeman broadening to quantify the surface magnetic field, one infers  $\langle |fB| \rangle = 40\text{--}160$  G starting from a solar value from run  $\mathcal{M}(\mathcal{A} = 1)$  of  $\sim 15$  G. A value of  $\sim 170$  G results from a calibration from Rossby number via Zeeman-Doppler imaging to an equivalent magnetic

flux density for a Zeeman broadening signal using Figure 1 and Eq. (2) in *See et al. (2019)*. Thus, the value of  $\sim 150$  G estimated above seems reasonable, although a substantial uncertainty should be allowed for.

A much more active star, but with otherwise solar parameters, is simulated using  $\mathcal{A} = 30$  in model  $\mathcal{M}(\mathcal{A} = 30)$ . The total flux on the stellar surface in the latter run peaks at about 7 times that of  $\mathcal{M}(\mathcal{A} = 1)$ : inserting more active regions with a given size spectrum leads to more flux cancellations, so that the total flux on the surface increases more slowly than linearly with the cycle strength (see, e.g., *Schrijver 2001*, for a discussion). Whereas it reaches a value of  $\langle |fB| \rangle$  commensurate with that of a star with  $P_{\text{rot}} \sim 12$  days, the rotational amplitude is too low (see Sect. 4).

To increase the rotational modulation, larger regions could be introduced. This also strengthens the impact of activity nests, the tendency for active regions to emerge within existing other regions or in sites of an earlier such emergence. Thus, another run,  $\mathcal{M}(\mathcal{A} = 30)^+$ , also with  $\mathcal{A} = 30$ , is created but with a maximum active-region flux per polarity of  $\Phi_{\text{max}}$  raised from  $1.5 \times 10^{22}$  Mx (as used in *Schrijver 2001*) to  $3 \times 10^{23}$  Mx. The latter value allows regions as large as that expected to power the Carrington-Hodgson flare to emerge (based on a flux estimate by *Aulanier et al. 2013*). Such very large regions are rare on the Sun (the largest region observed to date, which occurred in April 1947, is estimated to have had a flux at that level, see *Taylor 1989; Schrijver et al. 2012*), hence the choice of  $\Phi_{\text{max}} = 1.5 \times 10^{22}$  Mx for the solar activity level in run  $\mathcal{M}(\mathcal{A} = 1)$ , but the occurrence of very large flares on more-active stars suggests that larger regions may be more common on such stars (see, e.g., *Maehara et al. 2012; Shibayama et al. 2013; Notsu et al. 2017*).

The model runs described above suggested that stars like Kepler-17 and WASP-36 may be approximated by a run of intermediate  $\mathcal{A}$  and  $\Phi_{\text{max}}$ , with parameters set as in run  $\mathcal{M}(\mathcal{A} = 10)^+$ . For comparison purposes, also a run  $\mathcal{M}(\mathcal{A} = 1)^+$  is executed for a star of solar activity, but allowing for large active regions, setting  $\Phi_{\text{max}} = 3 \times 10^{23}$  Mx.

Note that all runs for an active Sun-like star with  $\mathcal{A} = 30$  have the same total amount of flux emerging per unit time in the range from  $6 \times 10^{18}$  Mx to  $1.5 \times 10^{22}$  Mx per polarity. The larger range of the power-law probability distribution for regions to be inserted into the stellar photosphere in runs with elevated  $\Phi_{\text{max}}$  introduces additional large regions, leading to more flux on the stellar surface, while maintaining the frequencies of the more abundant smaller regions to match the shape of the size spectrum derived from solar observations (while allow-

ing an overall multiplicative factor). Given the properties of the active-region frequency distribution, the rate of flux input for  $\Phi_{\text{max}} = 3 \times 10^{23}$  Mx is increased by a factor of 1.7 relative to  $\Phi_{\text{max}} = 1.5 \times 10^{22}$  Mx. Larger regions disperse more slowly, which also leads to increased persistence of successive generations of flux emergence within them (in active-region nests), so that the total amount of flux in the photosphere increases more than the rate at which flux input increases if the spectrum is extended to higher fluxes (see Table 2).

To bootstrap the simulation runs relatively quickly into a state in which the polar caps are less sensitive to the initial state (an empty stellar surface), for all runs except  $\mathcal{M}(\mathcal{A} = 30)^+$ , half of all flux concentrations is randomly removed after the completion of the first 11-yr sunspot cycle (using the same procedure as in *Schrijver and Title 2001*). For these runs, the data shown here are taken from the third sunspot cycle, i.e., covering the years 22 to 33 for the simulations. Any effects of the initial state or the removal of half of all concentrations after the first 11 years are moreover dampened by the half-life decay time scale of flux concentrations of 5 yr. For run  $\mathcal{M}(\mathcal{A} = 30)^+$ , when the code is tracking over  $2 \times 10^5$  elements near cycle maximum, the  $n^2$  nature of the algorithm testing for collisions between flux concentrations leads to much longer computation time; as only the high-latitude fields require a multi-decade run, while these have little impact on the transit residuals being studied, for this run data are shown in the same cycle phases as for the others, but from the first rather than third sunspot cycle.

Sample simulation results for the magnetic field distributions across the stellar surface are shown in Figures 1a-1d. As the focus of this study is the signal from exoplanetary transits, and as most planetary systems appear to have their normal vector rather well aligned with the stellar rotation axis, the perspective for visualizations of these simulations is chosen to lie in the plane of the stellar rotational equator.

### 3.3. Modeling photospheric appearances

Estimation of the brightness of facular patches on the faces of stars requires knowledge of their contrast as a function of viewing angle (or relative distance from disk center), wavelength, and corresponding characteristic absolute magnetic flux densities. Here, disk appearance, rotational modulation, and transit signals are simulated for three wavelengths for which *Norris et al. (2017)* show facular contrast versus limb distance (their Fig. 8) and activity level: 3870 Å, 6010 Å, and 15975 Å. Their values are based on magnetoconvective calculations with radiative transfer using the MURaM code,

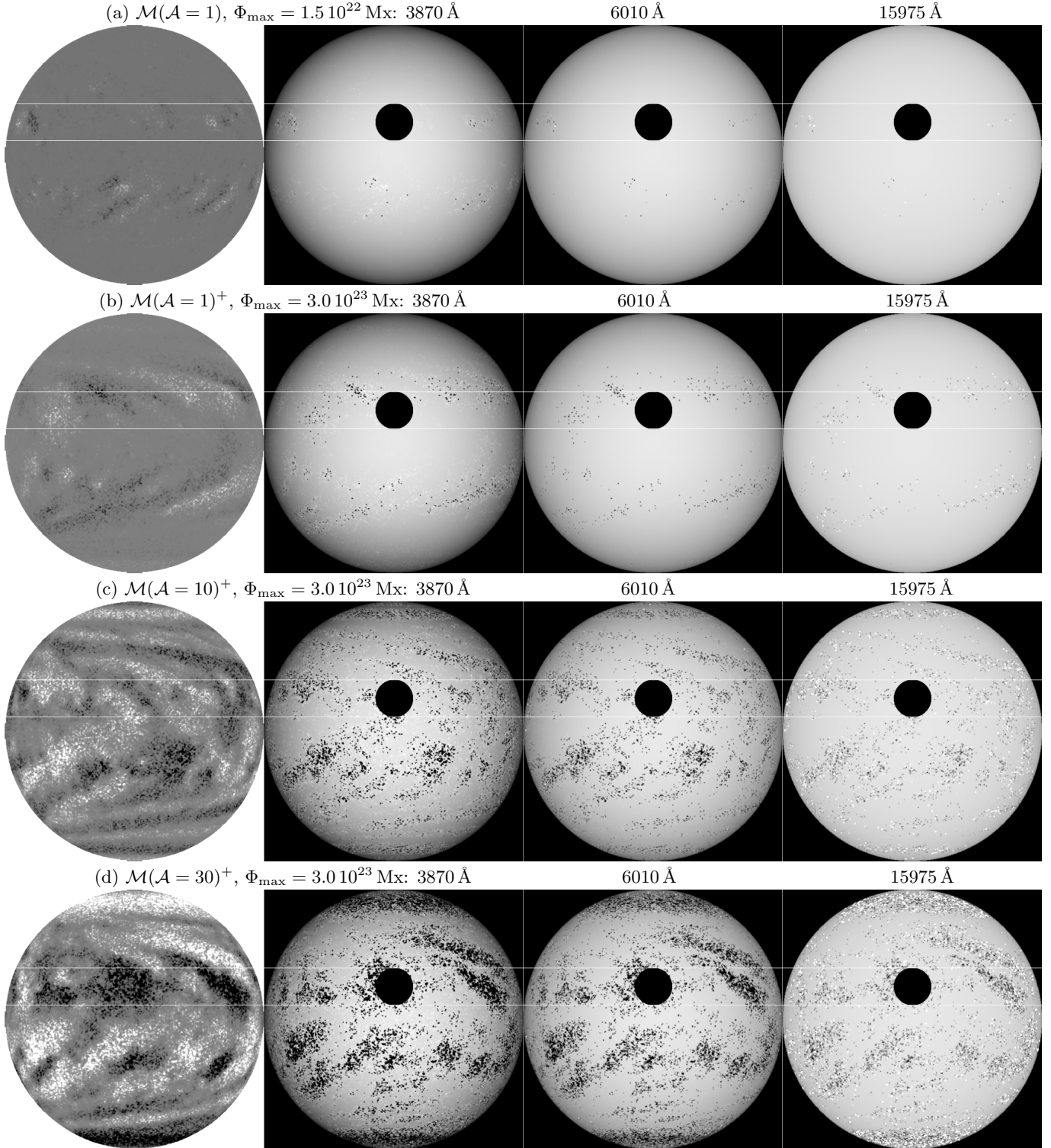


**Figure 1.** Simulated magnetograms (left panels; gray scale saturates at  $\pm 1.35$  kG) and intensity images for 3870 Å, 6010 Å, and 15975 Å, respectively, for a Sun-like star, approximately 5.5 yr after the minimum in its solar-like sunspot cycle. The intensity contrast relative to the quiet photosphere has been doubled to better show the faculae. The cycle amplitude  $\mathcal{A}$  and the maximum flux  $\Phi_{\max}$  per polarity in the largest active regions (see Sect. 3.2 for their definition) are indicated above the magnetograms. The transit path and the exoplanet size used in Sect. 5 are shown by white lines and the black disks.



validated successfully against solar observations.<sup>3</sup> For values of  $\mu$  between 0 and 0.2, close to the limb, for which they show no results, a smooth transition to zero contrast at the limb is imposed.

The background limb darkening of the quiet photosphere is set to that measured by Neckel and Labs (1994), except for the 15975 Å channel for which I use the polynomial fit to the data presented in Figure 4 by Norris *et al.* (2017).

To estimate the average magnetic flux density to be used to compute facular brightenings, I assume that the flux in a model concentration is spread out over an area with a radius equal to the coagulation radius of  $r_c = 4200$  km: concentrations that approach each other closer than that in the model are considered to merge. The flux threshold at which bright faculae transition to dark pores or spots is set to  $\Phi_b = 3 \times 10^{20}$  Mx (see Table 4.1 in Schrijver and Zwaan 2000).

For spots, the average intrinsic field strength over the combined area of umbra and penumbra is set to 1.35 kG based on the study by Solanki and Schmidt (1993), who note that this value is similar to the field strength characteristic of smaller magnetic features; this value is therefore used as intrinsic field strength in the visualizations here for all flux concentrations. For the intensity contrast averaged over an entire pore or spot, I assume an average intensity contrast derived from the ratio of blackbody temperatures of the spot and photosphere,  $T_{\text{spot}}$  and  $T_{\text{phot}}$ , respectively, corresponding to the wavelength  $\lambda$  considered:  $c_s(\lambda) = (\exp(hck/(\lambda T_{\text{phot}})) - 1) / (\exp(hck/(\lambda T_{\text{spot}})) - 1)$ , for  $h$  the Planck constant,  $c$  the speed of light in vacuum, and  $k$  the Boltzmann constant. Radiative transfer effects for different wavelengths are ignored in the present approximation.

For the Sun-like star simulated here, the photospheric temperature is set to  $T_{\text{phot}} = 5780$  K. For the effective temperature of the spot area, including umbra and penumbra, I use  $T_{\text{spot}} = 5150$  K as inferred from solar irradiance modeling by Fligge *et al.* (1998, see also, *e.g.*, Fligge *et al.* (2001)). More recent modeling may include umbral and penumbral components separately, such as in the study by Unruh *et al.* (2008) which uses a penumbral temperature of 5150 K and an umbral temperature of 4500 K. However, as the penumbral area dominates umbral areas by factors of typically 3:1 (Fligge *et al.*

1998) to 5:1 (Martinez Pillet *et al.* 1993), using a single, largely penumbral temperature as characteristic for the overall spot output suffices for the present purpose. With these values for  $T_{\text{phot}}$  and  $T_{\text{spot}}$ , the spot brightness relative to the photosphere at 3870 Å, 6010 Å, and 1.6 μm is 0.45, 0.60, and 0.79, respectively. The same relative limb-darkening curve is assumed as for the quiet photosphere at the wavelength under consideration.

Each flux concentration is mapped into the image pixel corresponding to its central location. For those with  $|\Phi_i| \leq \Phi_b$ , the effective radius  $A_{\text{eff}}$  is assumed to be  $r_c$ . For concentrations with  $|\Phi_i| > \Phi_b$ , an area of  $A_\Phi = |\Phi_i|/B_{\text{phot}}$ , with  $B_{\text{phot}} = 1.35$  kG is assumed to hold for the average field strength over the combined umbral and penumbral areas. For the concentrations for which  $A_\Phi$  exceeds the unprojected surface area mapping into an image pixel, the area is approximated as a foreshortened circular disk (pixelation effects are corrected for by matching the total intensity in a disk to the area mapped onto an image array). For fractional pixels, and for concentrations for which the area  $A_{\text{eff}}$  is smaller than the solar surface area under an image pixel, the intensity in that pixel is modified using the fraction of the pixel area covered by the magnetic concentration, assuming the intensity of the complement of that pixel area is unaffected.

Simulated magnetograms are made by mapping the fluxes  $\Phi_i$  of the flux concentrations onto an image, spread out over disks with radius  $A_\Phi$ , and subsequently modified with a multiplicative factor for each pixel equivalent to assuming that the magnetic field is normal to the local surface.

Sample simulation results for the intensity images at three different wavelengths are shown in the right-hand three panels of Figures 1a-1d (with doubled contrast to better show the faculae). The images in these figures were smoothed with a Gaussian with a FWHM value of 2 pixels. The images show that both the facular contrast and the spot contrast are largest for the shortest wavelengths, as expected from the facular contrasts and the wavelength-dependent contrast  $c_s(\lambda)$ . And, also as expected, the faculae stand out most clearly toward the limb while spots and pores are most readily visible toward the central regions of the disks.

One property that jumps out in particular in the intensity images of Figures 1c-1d is the abundance of dark features with diameters of order 8000 km. This is a consequence of the numerical prescription for the fractionation probability of flux concentration. This has a local minimum (and thus a corresponding maximum in the lifetime) around  $10^{21}$  Mx. Consequently, clusters of such solar-like spots develop in the model. While this

<sup>3</sup> The applicability of these models to stars substantially more active than the Sun is supported by, *e.g.*, the observations by Linsky *et al.* (2012) who conclude that the thermal structure and heating rates inferred for active stars are comparable to those of the brightest solar faculae (see Linsky 2019, for a broader discussion).

fractionation probability approximates the behavior of most sunspots well, it is as yet unknown how spots and spot clusters behave in very active stars or extremely large bipolar regions (if these indeed exist). Numerical experiments with radiative magnetoconvection by [Beek et al. \(2015a,b\)](#), however, suggest that in the presence of an increasingly strong field, (micro-)pores are a naturally occurring phenomenon for cool main-sequence stars when the mean flux density exceeds a few hundred  $\text{Mx}/\text{cm}^2$ . This may or may not be what happens on a very active star, but even if it does not happen, compact clusters of such spots in the model run here may effectively describe the appearance of any large spot in real life from the point of view of rotational modulation or transit signals for planets of a size comparable to Jupiter as simulated here. Note that the images shown in Figures 1a–1d have a best effective resolution of 5500 km at disk center (given the diameter of the rendered images of 512 pixels subjected to a Gaussian smoothing with FWHM of 2 pixels), to be compared to  $r_c = 4200$  km.

Another feature that stands out in Figures 1c–1d is the multitude of spots and pores that persist in the poleward arcs formed by decaying active regions, and also in flux dispersal toward the equator. In the models, these dark features are the result of the frequent collisions and temporary mergers between flux concentrations in regions of high average flux density. Such high flux concentrations on the Sun would correspond to pores and small spots.

#### 4. OUT-OF-TRANSIT BRIGHTNESS AND ROTATIONAL MODULATION

This section reviews how the modeled stars would be viewed in terms of brightness and rotational modulation in the absence of exoplanetary transits. Only a single realization is randomly selected for this study (5.5 yr after a minimum, and 1.5 yr after the maximum in the simulated cycle), which focuses on trends in its testing of the solar paradigm against selected observations.

##### 4.1. Net brightness

First to discuss is the average relative offset  $\delta_* = (I_*(\infty, \lambda) - I_q(\lambda))/I_q(\lambda)$ , where  $I_*(\infty, \lambda)$  is the brightness of the active star out of transit and  $I_q(\lambda)$  is that of the quiet-star (here quiet-Sun) photosphere. Values for  $\delta_*$  are listed in Table 2. Note that these values should be compared across wavelength for a given set; substantial statistical fluctuations make these values less suitable for comparison between runs, although the trends are likely to stand. These values show that the tradeoff between bright faculae and dark spots is such that the overall brightness of a star with Sun-like activity ( $\mathcal{M}(\mathcal{A} = 1)$ ) is increased during cycle phases of enhanced activity relative to the reference quiet Sun. The averaged contrast

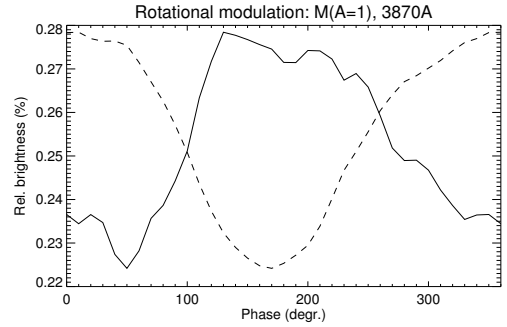


**Figure 2.** Solid line: rotation modulation for 3780 Å for run  $\mathcal{M}(\mathcal{A} = 1)$ , as viewed from the rotational equator, and expressed as a difference compared to an inactive but limb-darkened photosphere such that phase angle  $0^\circ$  (corresponding to the images in Fig. 1a) shows the offset  $\delta_*$  from Table 2. Dashed line: total flux on the observer-facing side of the star, rescaled to the same amplitude as the intensity but inverted in sign.

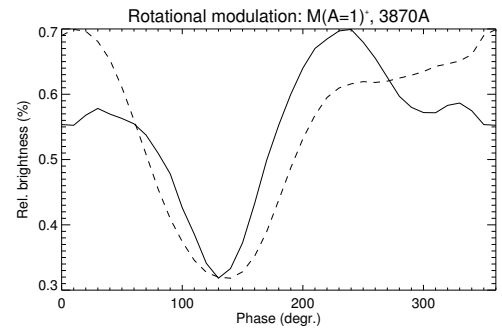


**Figure 3.** As Figure. 2 for  $\mathcal{M}(\mathcal{A} = 1)^+$ .

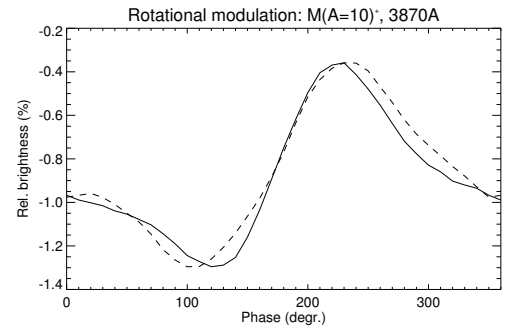


**Figure 4.** As Figure. 2 for  $\mathcal{M}(\mathcal{A} = 10)^+$ .

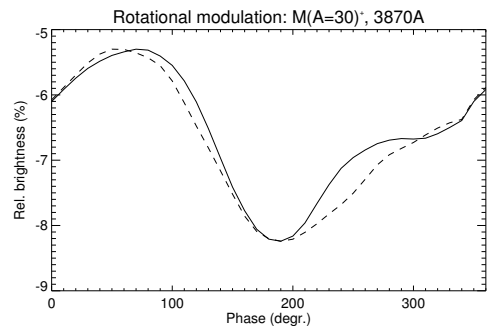


**Figure 5.** As Figure. 2 for  $\mathcal{M}(\mathcal{A} = 30)^+$ .

**Table 2.** Model properties and modulation estimates. The table lists the following for a single, arbitrarily-chosen step in the flux-transport model for an activity phase about 1.5 yr after cycle maximum, following the run identifier, which includes the cycle-strength factor  $\mathcal{A}$ , and the maximum active-region flux per polarity  $\Phi_{\max}$ : globally-averaged absolute magnetic flux density  $\langle |fB| \rangle$  of all flux elements and  $\langle |fB| \rangle_{\text{fac}}$  for the faculae (with fluxes below  $3 \cdot 10^{20}$  Mx); globally-averaged areal filling factor  $f_d$  of dark pores and spots assuming an intrinsic field strength of 1.35 kG; the contrast  $\delta_*$  of the total unocculted brightness of the active star and the unocculted inactive star from the perspective shown in Figure 1; peak-to-trough rotational modulation, and – in the final set of three columns – peak-to-trough amplitude  $\Delta(\lambda)$  for the transit residuals, both as shown in Figures 1a–1d. Note that  $\delta_*(\lambda)$  and  $\Delta(\lambda)$  are for rough intercomparison only as they are computed for a single time step in the flux-dispersal model and for a transit across a single viewing angle of the stellar sphere.

Run	$\Phi_{\max}$ ( $10^{22}$ Mx)	$\langle  fB  \rangle,$ $\langle  fB  \rangle_{\text{fac}}$ (G)	$f_d$ (%)	Net Intensity Change $\delta_*$ (%)			Rotation Modulation (%)			Transit Residual Ampl. $\Delta(\lambda)$ (ppm)		
				3870	6010	15975	3870	6010	15975	3870	6010	15975
$\mathcal{M}(\mathcal{A} = 1)$	1.5	16, 15	0.06	+0.24	+0.04	+0.014	0.06	0.014	0.010	180	40	40
$\mathcal{M}(\mathcal{A} = 1)^+$	30	60, 51	0.65	+0.55	−0.01	−0.00	0.38	0.31	0.12	420	180	70
$\mathcal{M}(\mathcal{A} = 10)^+$	30	212, 132	5.9	−0.97	−1.60	−0.40	0.90	0.64	0.25	980	520	300
$\mathcal{M}(\mathcal{A} = 30)$	1.5	135, 100	2.6	+0.26	−0.54	−0.12	0.30	0.22	0.08	1100	540	190
$\mathcal{M}(\mathcal{A} = 30)^+$	30	479, 175	22.	−6.1	−5.3	−1.3	2.9	2.0	0.7	6300	3800	1400

over the three wavelengths, used as a rough proxy for the bolometric value, is  $\sim 0.1\%$ . This value compares well with the observed change in total solar irradiance over the cycle (*e.g.*, Fröhlich 2016; Kopp 2016).

For the simulations of the more-active stars, the faculae play a relatively weaker role than starspots, resulting in a dimming of the overall stellar brightness. For  $\mathcal{M}(\mathcal{A} = 1)^+$  this results in a near balance between spot darkening and facular brightening for the longer wavelengths, while for the most active star, simulated sunspot darkening outweighs facular contributions at all three model wavelengths. This trend is consistent with the empirical results of Lockwood *et al.* (1997) and Radick *et al.* (2018, see also Montet *et al.* (2017)). In their long-term monitoring of a set of cool stars, they note that more-active stars tend to dim as chromospheric activity increases due to dynamo variability, suggesting a dominant role of starspots over faculae. In contrast, for many less-active stars – including the Sun – photospheric brightness increases with increasing activity, which is interpreted to be owing to a stronger role of faculae relative to that of spots, although the latter can cause dips in the brightness when crossing near central meridian due to solar rotation.

Figure 15 by Radick *et al.* (2018) suggests that spots and pores dominate in irradiance variations beyond a chromospheric activity level of  $\log(R'_{\text{H+K}}) \approx -4.75$ , compared to a characteristic solar value of around  $-4.9$ . Converting the level of  $\log(R'_{\text{H+K}}) \approx -4.75$  into an  $S$ -index value (Noyes *et al.* 1984), and applying Eqs. (1) and (2) in Shapiro *et al.* (2014) yields a corresponding spot/pore filling factor of 1.2% and a facular filling factor of 6.8%, which with  $B = 1.35$  kG yields  $\langle |fB| \rangle \approx 100$  G for spots/pores and faculae combined.

This appears compatible with the summary results in Table 2.

#### 4.2. Rotational modulation

To compute the rotational modulation as shown by the solid curves in Figures 2–5, the perspective of the rendered photospheres is changed, but the magnetic field is held frozen in time (phase angle  $0^\circ$  corresponds to the images shown in Figures 1a–1d). Dashed curves in these figures show the total magnetic flux on the observer-facing side of the star, rescaled to the same range for comparison, and inverted in sign because more flux is generally due to more active regions that put more spots and pores on the star, except in run  $\mathcal{M}(\mathcal{A} = 1)$  where brightness and magnetic flux on a hemisphere are positively correlated.

This single snapshot of rotational modulation clearly is only one of many instantiations of the field distribution, but gives an idea of the magnitude of the modulations that is sufficient for the present purpose. The amplitude of rotational modulation for the simulation of the Sun-like star ( $\mathcal{M}(\mathcal{A} = 1)$ ) at  $4000 \text{ \AA}$  is  $\sim 0.06\%$ . This single example of rotational modulation lies only somewhat below the value of  $\approx 0.1 - 0.2\%$  characteristic of the active Sun (Fröhlich 2016; Lee *et al.* 2016).

On the one hand, this single snapshot model is at least roughly of comparable magnitude to observations. On the other hand, the rotational modulation of more-active stars also comes out low if only the emergence frequency, but not the size spectrum, of active regions is changed. For  $\mathcal{M}(\mathcal{A} = 30)$ , the rotational modulation at visible wavelengths is  $\sim 0.2\%$ . This is considerably weaker than what is observed in stars of correspondingly high activity. One example is the rotational modulation observed for Kepler-17 (Table 1) which is about 1–2%. Other ex-

amples of stars with comparable rotation periods can be found in Notsu *et al.* (2013) for a sample of stars that exhibit superflaring in the *Kepler* data: typical amplitudes of rotational brightness modulation for such stars fall in the range from 1% to 5%, with most clustering around 2%.

There are two ways by which the model’s rotational modulation can be increased: raise the frequency of emergence of active regions, or allow for larger active regions to emerge. The frequency spectrum for emerging bipoles used in the present simulations is based on the work by Harvey and Zwaan (1993), and is thus characteristic of sunspot Cycle 21. Without guidance on, for example, preferred longitudes for flux emergence, statistically, one expects an increase in rotational modulation that scales as the square root of the number of regions (see also Rackham *et al.* 2018). Based on this, rather than modifying this frequency or introducing longitudinal patterns in an ad hoc fashion, the second possibility is explored. The largest active regions that emerged in the 846-day period of observations analyzed by Harvey and Zwaan (1993) had a total absolute magnetic flux per polarity of roughly  $4 \times 10^{22}$  Mx, with only a single occurrence of such a large region during the period of their analysis. This led Schrijver (2001) and Schrijver and Title (2001) to set  $\Phi_{\max} = 1.5 \times 10^{22}$  Mx in their model runs to stay just below the most uncertain part of the active-region size spectrum with infrequent realizations on the Sun.

A later study by Zhang *et al.* (2010), spanning a longer period, showed regions with fluxes up to about  $3 \times 10^{23}$  Mx per polarity. When the flux-emergence spectrum is extended to this flux for a star of otherwise solar properties (in run  $\mathcal{M}(\mathcal{A} = 1)^+$ ), the rotational modulation at visible wavelengths reaches  $\sim 0.3\text{--}0.4\%$ . This certainly lies in the range of solar rotational modulation, but now the added flux leads to surface-averaged flux densities that are too high (Table 2). Without experimenting further in the present context, I hypothesize that there may be a decline in active-region frequencies for region with fluxes approaching  $3 \times 10^{23}$  Mx, dropping below the power law seen at lower fluxes. This would be in line with comments by Zhang *et al.* (2010), and with the occurrence of infrequent but large regions discussed by Schrijver *et al.* (2012), while occasionally resulting in larger rotational modulation and also regions large enough for infrequent powerful solar flares (Aulanier *et al.* 2013).

The result of allowing larger regions is also noticeable for the more-active stars: the rotational modulation found for  $\mathcal{M}(\mathcal{A} = 10)^+$  and  $\mathcal{M}(\mathcal{A} = 30)^+$  with  $\Phi_{\max} = 3 \times 10^{23}$  Mx, is significantly larger than for

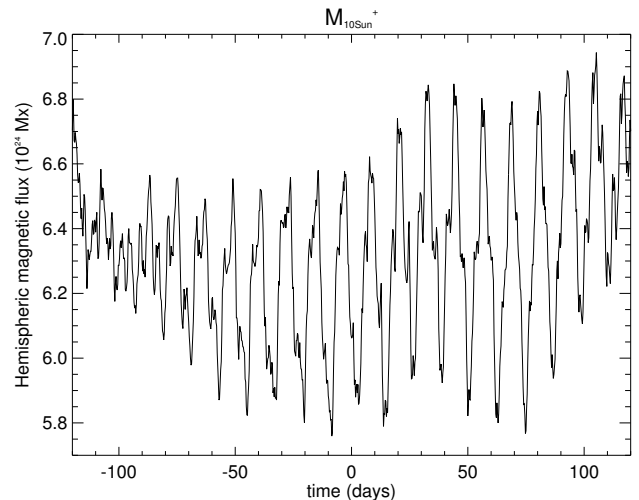


**Figure 6.** Total magnetic flux on the observer-facing side of the star modeled in run  $\mathcal{M}(\mathcal{A} = 10)^+$ , assuming a synodic rotation period of 12 days at the Carrington reference latitude of  $16^\circ$ . The interval shown extends over 20 rotation periods, with the time  $t = 0$  set to the reference time for which Figures 1c and 4 are shown, at the full temporal resolution of the model of 6 hr/step.

$\mathcal{M}(\mathcal{A} = 30)$ , reaching roughly 1–3% in the visible. Not only are these models in the range of the observed rotational modulation of Kepler-17 and other similar *Kepler* targets, but they also inject bipoles of sufficient magnitude to power the occasional superflares observed on such stars (*e.g.*, Schrijver *et al.* 2012; Aulanier *et al.* 2013; Notsu *et al.* 2013).

Model  $\mathcal{M}(\mathcal{A} = 30)^+$  has an average magnetic flux density of  $\langle |fB| \rangle \sim 500$  G (Table 2). Notsu *et al.* (2015) show a trend of increasing  $\langle |fB| \rangle$  versus the amplitude of the rotational brightness variation (their Figure 8b). They base this scaling on solar observations of the Ca II infrared triplet compared to a magnetogram, and measure the stellar Ca II infrared triplet to establish the mean stellar level of activity. If only the total flux in facular elements (with fluxes below  $3 \times 10^{20}$  Mx) is taken to contribute in the Ca II triplet, then for model values of  $\langle |fB| \rangle_{\text{fac}} \approx 180$  G the scaling found by Notsu *et al.* (2015) would map to brightness variation amplitudes by rotational modulation of  $\approx 1.5\%$ , which compares well with what is found here (Table 2).

The rotational modulation is the result of the inhomogeneous distribution of magnetic flux across the stellar surface, with the signal presenting a mean over entire hemispheres. The result is a relatively smooth curve as a function of the phase angle, as shown in Figures 2–5. The hemispheric smoothing can result in a simple modulation often at the apparent period of rotation (Figures 4 and 5), but for the less-active stars rotation periods can

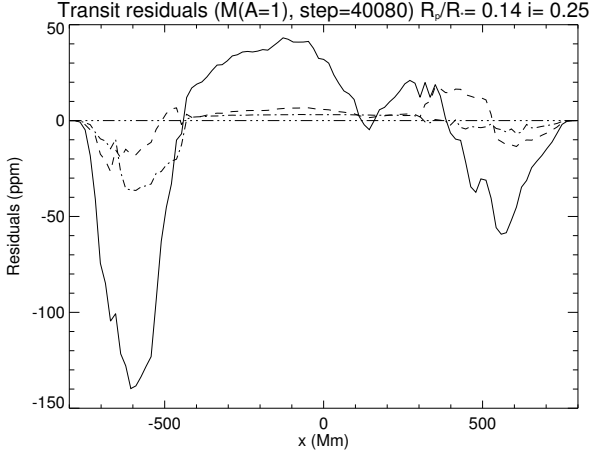


**Figure 7.** Transit residuals normalized to the out-of-transit signal for  $3780 \text{ \AA}$  (solid),  $6010 \text{ \AA}$  (dashed), and  $15975 \text{ \AA}$  (dash-dotted) for an instance in  $\mathcal{M}(\mathcal{A} = 1)$  (corresponding to a phase angle of  $0^\circ$  in Fig. 2). The time steps used for the transit correspond to  $\approx 16 \text{ Mm}$  in the plane of the sky.

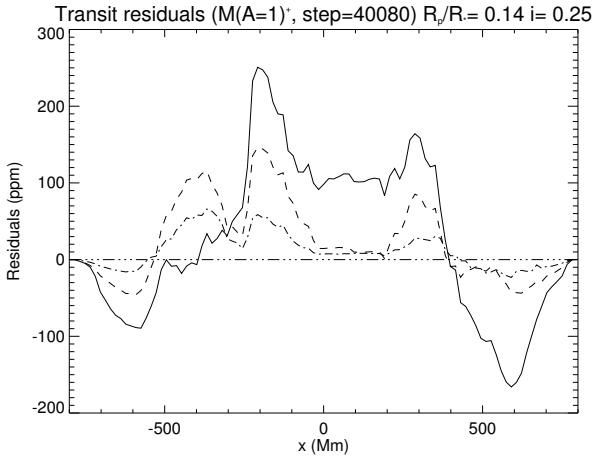


**Figure 8.** As Fig. 7 for  $\mathcal{M}(\mathcal{A} = 1)^+$ .

be masked. The appearance of observed light curves of active stars may suggest the existence of only a few large spot groups, but the images in Figures 1a–1d suggest that the real situation may be far more complex.

Figure 6 illustrates the rotational modulation over time by looking at the total amount of magnetic flux on the ‘observer-facing’ hemisphere of the ‘rotating star’: here, the magnetic evolution is shown for run  $\mathcal{M}(\mathcal{A} = 10)^+$  over a total of 20 simulated rotation periods set to 12 days each, at the full model resolution of its 6 hr steps, centered on the time shown in Figure 1c. The figure shows a clear long-term evolution in the total amount of flux, but for most of the period there is a pronounced rotational modulation suggestive of a dominant active hemisphere where none is prescribed in the model.

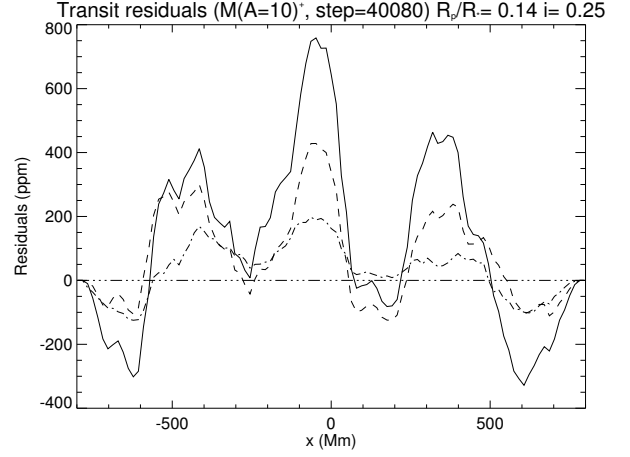


**Figure 9.** As Fig. 7 for  $\mathcal{M}(\mathcal{A} = 10)^+$ . Compare to Figure 11 where a series of transits are shown for  $3870 \text{ \AA}$  for different rotation angles of the simulated star.

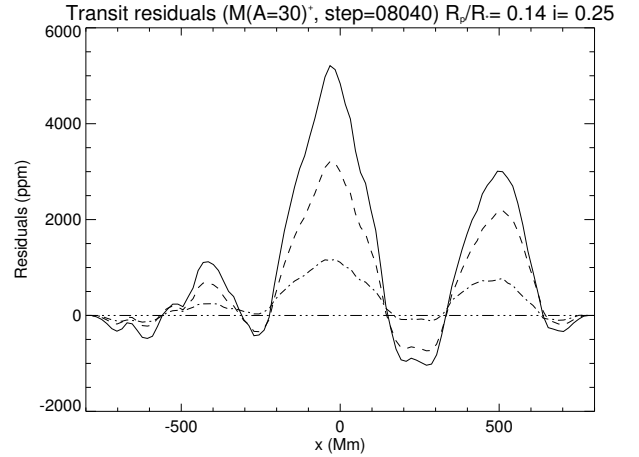


**Figure 10.** As Fig. 7 for  $\mathcal{M}(\mathcal{A} = 30)^+$ .

## 5. TRANSIT SIGNALS

### 5.1. Aspects of model transit light curves

The average radius of the selected exoplanets in Table 1 is  $0.14R_*$ , which is also characteristic of WASP-36b and Kepler-17b, which orbit the most Sun-like stars of the longest rotation periods in the sample listed. In the transit simulations discussed here, I therefore adopt a planetary radius of  $0.14R_\odot$ . Smaller virtual exoplanets can, of course, also be used, but that is an application that can await both advanced magnetoconvective models of stellar photospheres and very large aperture telescopes with increased S/N properties. One exception is made for comparison to a transit with a planetary radius of  $0.02R_\odot$  discussed below.

Figures 1a–1d show examples of transits paths across the model stars with a relative impact parameter for the transit of  $d_t = 0.25R_*$  (compare with the estimated

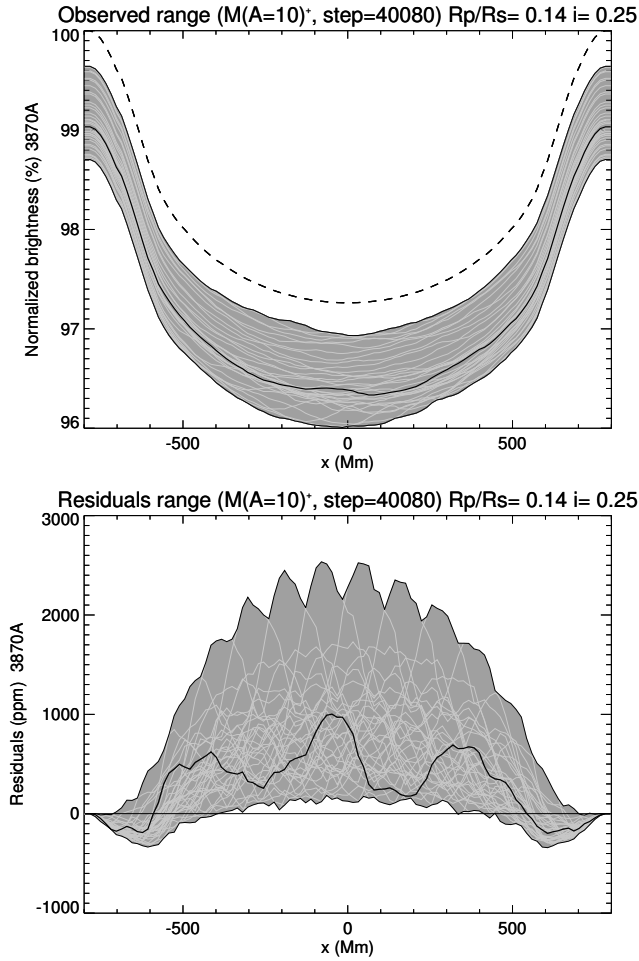


**Figure 11.** (top) Transit signal and (bottom) transit residuals as for Figure 9 for run  $\mathcal{M}(\mathcal{A} = 10)^+$  for 3870 Å and  $R_p/R_* = 0.14$ , shown by the thick black curve. Transit signals are computed for a series of different perspectives, rotating the star each time by  $10^\circ$ . In the top panel, all transit signals are normalized to the intensity of the inactive star. In the bottom panel, all residuals are shifted to a zero value out of transit. The shaded band shows the range of signals; note that the peaks in the upper envelope in the bottom panel are a result of the stepping by  $10^\circ$ . The light grey curves depict the transit residuals for each of these viewing angles. The dashed black line in the top diagram shows the transit signal for an inactive photosphere.

values for the selected stellar sample in Table 1), for which Figures 7–10 show the transit residuals, calibrated relative to the inactive star and to zero out of transit:

$$\mathcal{R}(t, \lambda) \equiv \frac{(I_*(t, \lambda) - I_q(t, \lambda))}{I_q(t, \lambda)} - \frac{(I_*(\infty, \lambda) - I_q(\infty, \lambda))}{I_q(\infty, \lambda)}, \quad (1)$$

where  $I_*(t, \lambda)$  is the modeled transit intensity at time  $t$  (running in the figures from first contact with the image field of view to fourth contact) and wavelength  $\lambda$ , and  $I_*(\infty, \lambda)$  is the brightness of the active star out of

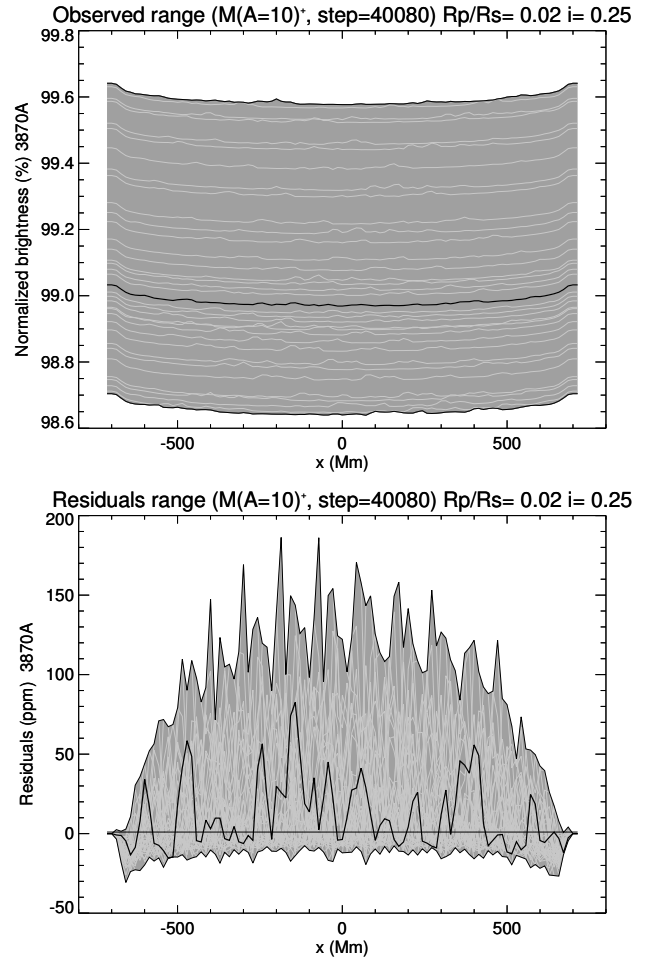


**Figure 12.** (top) Transit signal and (bottom) transit residuals as for Figure 11, but for a transiting planet with  $R_p/R_* = 0.02$  (or  $\sim 2R_\oplus$ ). In this case, the rotational modulation far exceeds the transit modulation, causing the apparently wide band in the top panel (note the difference in vertical scale with Fig. 11).

transit;  $I_q$  are the same for the quiet, featureless photosphere. The curves are fairly smooth for two reasons: the random-walk diffusion of the magnetic flux leads to relatively smooth gradients in the surface field, with further smoothing imposed by the exoplanet diameter. But there are fine-scale variations that, if they are detectable in real observations, could be used to study structural details of stellar magnetic fields, provided that the effective telescope aperture is sufficiently large to keep exposures short while obtaining a high S/N ratio.

Figures 7–10 show only a single instance of an arbitrarily chosen step in the flux-transport simulations and a single viewing angle, while comparing the residuals for the three wavelengths used here. Figure 11 provides an impression of the full range of transit curves (top panel) and transit residuals (bottom panel) for

run  $\mathcal{M}(\mathcal{A} = 10)^+$  (compatible with a Sun-like star at  $P_{\text{rot}} \approx 12$  days) for only  $3870 \text{ \AA}$  computed by rotating the star underneath a series of transits. The full range of transit residuals for this time step clearly shows the effect of limb brightening by faculae in the dips early and late in the transits. Moreover, the full range of residuals is more than double the amplitude of the single realization selected for Figure 9. For comparison, Figure 12 shows the simulated transit signals and residuals for a much smaller planet ( $R_p/R_* = 0.02$ ); note that for such a small planet umbral-penumbral differences – here ignored – are in principle accessible, although this would require S/N levels that are currently unaccessible.

All transit residuals reveal signatures of the facular brightening toward stellar limbs, recognized as dips near the beginnings and ends of the transit residuals (to be compared, for example, to a similarly shaped transit light curve for Kepler-71 shown in Figure 4 of Zaleski *et al.* 2019). This is in effect a wavelength- and activity-dependent distortion of the limb-darkening curve (which should be anticipated to be asymmetric because the stellar activity along the transit path is expected to be generally asymmetric).

Next, I consider the magnitude of the residuals: The peak-to-trough ranges in the transit residuals,  $\Delta(\lambda)$  (summarized in Table 2) confirm the very weak transit signals expected for a star of solar activity,  $\mathcal{M}(\mathcal{A} = 1)$ , even when allowing for large active regions as in  $\mathcal{M}(\mathcal{A} = 1)^+$ . For the stars listed in Table 1 with rotation periods in the range of 8–12 days, transit-residual amplitudes reach values of up to 0.15–0.4%. These values are much larger than those found for  $\mathcal{M}(\mathcal{A} = 30)$ , but are compatible with the model results for  $\mathcal{M}(\mathcal{A} = 10)^+$  and  $\mathcal{M}(\mathcal{A} = 30)^+$ , *i.e.*, for models in which much larger active regions are included in the emergence spectrum.

Figures 1c and 1d reveal the consequences of raising  $\Phi_{\text{max}}$  to  $3 \times 10^{23} \text{ Mx}$ : the injection of very large regions leads to a larger length scale in the flux patterns (compared to solar patterns as in Figure 1a), and these large areas of high magnetic flux densities are conducive to forming or maintaining concentrations with high magnetic fluxes, many of which appear as spots and pores. At least that is what happens in the models based on the properties derived from solar observations.

### 5.2. Estimating the planetary radius

The effective area of the occulting disk relative to that of the background star, based on the relative occultation depth  $d(t, \lambda) = 1 - I_*(t, \lambda)/I_*(\infty, \lambda)$  at any time  $t$  during the transit can be expressed as follows:

$$\frac{R_p^2(\lambda)}{R_*^2(\lambda)} = d(t, \lambda) \left( \frac{I_*(\infty, \lambda)}{I_o(\mathbf{r}(t), \lambda)} \right), \quad (2)$$

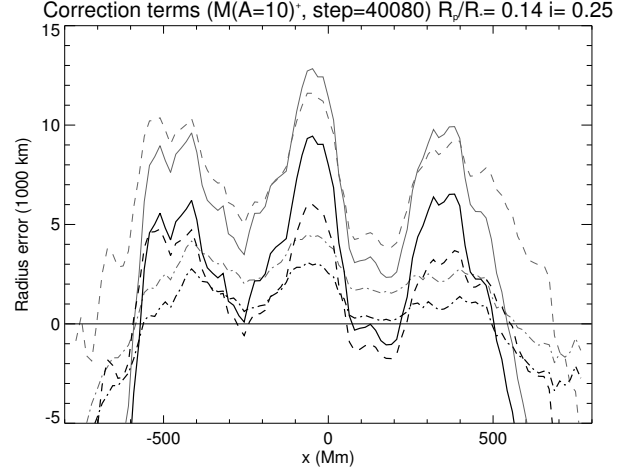


**Figure 13.** Activity-related terms for estimated planetary radius for a transiting planet with  $R_p = 1.4R_{\text{Jup}}$  based on the effects of stellar surface activity as captured in Eq. (5). The curves shown (as a function of the distance  $x$  from central meridian measured against the plane of the sky) match the transit residuals as shown in Figure 7, *i.e.*, for model  $\mathcal{M}(\mathcal{A} = 10)^+$ ; solid for  $3870 \text{ \AA}$ , dashed for  $6010 \text{ \AA}$ , and dash-dotted for  $1.6 \mu\text{m}$ . Thin gray lines show the magnitude of the final term in parentheses in Eq. (5), while the thick black lines also include the overall brightness term with  $\delta_*(\lambda)$  as shown in Table 2.

where  $I_o(\mathbf{r}, \lambda)$  is the mean intensity of the patch occulted by the transiting exoplanet and  $I_*(\infty, \lambda)$  is the overall mean stellar intensity out of transit. Below, any wavelength dependence of  $R_*$  is ignored.

Determining the deceptively simple-looking ratio  $I_*(\infty, \lambda)/I_o(\mathbf{r}(t), \lambda)$  is a challenge: we do not know what is masked by the exoplanet, and what is important in the ratio is the difference between the surface structures on the entire observer-facing side of the star and that occulted by the planet, including limb darkening, which is relatively poorly known compared to that to which we have some observational access, namely along the transit path, and there is contaminated by surface activity.

Having observations at multiple wavelengths will help in constraining spot and plage contributions to the stellar brightness over the spectrum, but not without more study. For example, the observed intensities  $I_*(\lambda)$  are related to the intrinsic intensity of a non-active star,  $I_q(\lambda)$ , the spot contrast and filling factor,  $c_s(\lambda)$  and  $f_s$ , and the facular brightness contrast across the surface,  $\mathcal{C}_f(\mathbf{r}, \lambda)$ , integrated over the observer-facing hemisphere, here with total area normalized to unity:

$$I_*(\lambda) = I_q(\lambda) \left( 1 + f_s c_s(\lambda) + \int \mathcal{C}_f(\mathbf{r}, \lambda) dS \right). \quad (3)$$

If the facular contrasts would have been essentially multiplicatively scaling functions across wavelength, *i.e.*, if

$C_f(\mathbf{r}, \lambda) \approx C_f(\mathbf{r})c_f(\lambda)$  for a contrast  $C_f$  at some reference wavelength associated with faculae only, then

$$I_*(\lambda) \approx I_q(\lambda) \left( 1 + f_s c_s(\lambda) + c_f(\lambda) \int C_f(\mathbf{r}) dS \right), \quad (4)$$

with the integral, independent of wavelength, a constant to be determined. Then the problem of determining the unknowns would have been a straightforward inversion problem. But the fact that the limb-brightening curves for faculae modeled by Norris *et al.* (2017) do not transform into one another by simple multiplicative factors implies that in order to fully disentangle the spot and facular components, the spatial distribution of these components across the stellar disk needs to be reasonably well known. For some purposes and some wavelengths, the approximation in Eq. (4) may suffice, but determining this is beyond the scope of this paper.

An estimate of the relative impact of the effect of the activity in the transit chord on the radius of the exoplanet and any surrounding atmosphere can be obtained by writing  $I_o(\mathbf{r}(t), \lambda) = I_q(\mathbf{r}(t), \lambda)(1 + \delta_o(\mathbf{r}(t), \lambda))$ , where  $I_q(\mathbf{r}(t), \lambda)$  is the quiet, limb-darkened photosphere behind the occulting planet and  $\delta_o(\mathbf{r}(t), \lambda)$  is the (spot plus faculae) relative difference in intensity of the occulted patch due to stellar activity. Similarly, we can write  $I_*(\infty, \lambda) = I_q(\infty, \lambda)(1 + \delta_*(\lambda))$ . For relatively small perturbations, so if  $\delta_o(\mathbf{r}(t), \lambda) \ll 1$  and  $\delta_*(\lambda) \ll 1$ , then Eq. (2) transforms into

$$R_p(\lambda) \approx R_*(\lambda) d^{\frac{1}{2}}(t, \lambda) \left( \frac{I_q(\infty, \lambda)}{I_q(\mathbf{r}(t), \lambda)} \right)^{\frac{1}{2}} \times \left( 1 + \frac{1}{2} \delta_*(\lambda) - \frac{1}{2} \delta_o(\mathbf{r}(t), \lambda) \right). \quad (5)$$

The final part of this equation essentially quantifies the ‘‘transit light source effect’’ related to stellar magnetic activity (*e.g.*, Rackham *et al.* 2018, 2019b).

Ignoring measurement uncertainties and assuming the quiet-star photospheric brightness, including limb darkening, is known, the final expression between parentheses in Eq. (5) quantifies the effect of stellar activity on the estimated planetary radius. Figure 13 shows an example of the overall impact on estimated values of  $R_p(\lambda)$  for a transiting exoplanet with radius  $1.4R_{\text{Jup}}$  for  $\mathcal{M}(\mathcal{A} = 10)^+$  by the last term in the final parenthetical expression of Eq. (5): in the near-IR, the impact is of order 2000–4000 km, while differences across wavelength from the blue to the near-IR amount to at least 1000 km even when times of minimal spot coverage are selected during the transit (thin gray lines in Figure 13).

If the wavelength-dependent impact of faculae and spots on overall brightness were known, *i.e.*, if we knew

$\delta_*(\lambda)$  – which we do in this case for the models – then this reduces the impact on the estimated planet radius in this example (thick black lines in Figure 13), depending on whether the transit covers sufficiently inactive photospheric regions. If, however, one were to use the amplitude of the rotational modulation along with the assumption that the asymmetry between hemispheres is entirely attributable to a single dominant spot group, and were to ignore facular contributions, then the estimated values for  $\delta_*(\lambda)$  would be substantially smaller than the true values, leading to wavelength-dependent errors equivalent to several 1000 km. For the other models in Table 2 these correction terms impact radius estimates from some 500 km in stars with solar-like activity ( $\mathcal{A} = 1$ ) to of order 5000 km at the high-activity end ( $\mathcal{A} = 30$ ).

## 6. DISCUSSION

Visual summaries of the results are provided in Figures 14 and 15. Figure 14 shows how the three different wavelengths respond to surface magnetic features as a function of modeled activity: generally, spot darkening exceeds facular brightening, except for stars of roughly solar activity level, where facular brightening overcompensates for spot dimming, particularly at the shortest wavelengths.

Figure 15 shows the general trend of increasing rotational modulation with transit residuals as well as of increased signals when larger active regions are included (both as anticipated). On the one hand, the signals for the selected stellar sample appear to lie somewhat above the values anticipated from the models for corresponding levels of activity  $\mathcal{A} \sim 10$  and rotation periods  $P_{\text{rot}} \sim 12$  days if allowing for large active regions. On the other hand, stellar data do follow the general trend defined by the models, even, for example, in the total average spot coverage of  $\approx 7\%$  for Kepler-17 derived from rotational modeling (Lanza *et al.* 2019) and  $\approx 5\%$  for WASP-52 based on a series of spectroscopic observations (Bruno *et al.* 2020) compared to the values  $f_d$  in Table 2. There are at least four possible interpretations: (1) the selected spot temperature was set too high or the selected average magnetic field strength to characterize umbral-plus-penumbra areas was set too low, (2) there is a selection bias in the stellar sample (and possibly in the transit residuals selected for display in the literature), such that the stars in the sample were studied for their transit signals precisely because these were strong, while on the other hand, the simulated models may have much stronger residuals when viewed from different perspectives than the randomly selected example that was analyzed (as is the case for Figures 11 and 12), (3) even



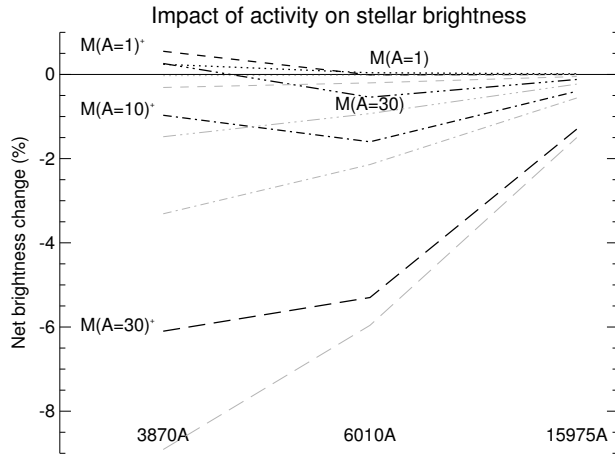


**Figure 14.** Visual summary of spectral impacts (from Table 2). Plotted are the values of  $\delta_*$ , the ratio of the brightness of the modeled active star relative to that of the reference quiet photosphere. The thick black lines show the effects of all surface activity, while the thin gray lines (using the same line patterns) include the effects of dark spots and pores alone.

larger active regions may need to be accommodated for, or (4) the overall level of stellar activity as characterized by  $\mathcal{A}$  from a rough calibration to the coronal brightness (see Sect. 3.1) needs to be raised somewhat, or some mix of the above. Possibly even the tidal effects between star and planet in these compact systems with heavy planets is important (Cuntz *et al.* 2000). All these aspects deserve further analysis in future studies. For now, we can also look at this diagram as quite encouraging because of the fair agreement of models and observations in view of the many unknowns going into the modeling.

Are the algorithmic elements of the model applicable to stars substantially more active than the Sun and to very large active regions? Lacking the necessary observational spatial resolution as well as guidance from magnetoconvective models, the present model results can only be tested against the transit and rotation-modulation observations to attempt to falsify the assumptions made.

The behavior of starspots presents one particular issue of interest. The code does not allow for very large spots to remain intact for very long, but rather will have such spots fragment, which, combined with collisional mergers working the other way, leads to the creation of clusters of dark features. Small clusters (or individual spots) would then lead to light-curve signatures that would be interpreted as compact and dark. In contrast, more extended clusters of spots in the model would lead to an observational signature that would be interpreted

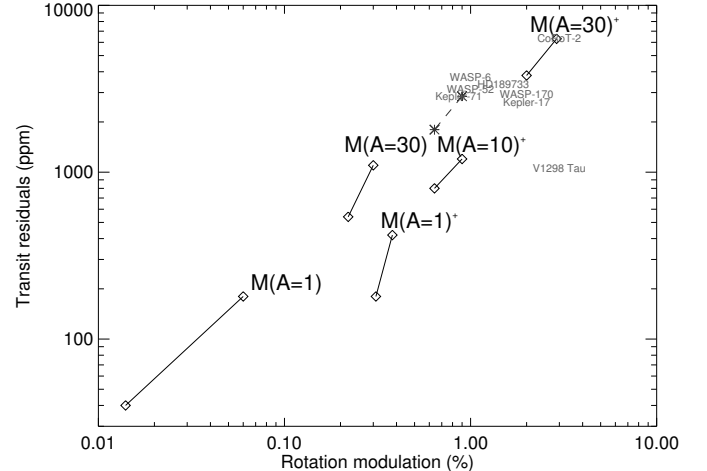


**Figure 15.** Visual summary of peak-to-trough transit residuals vs. peak-to-trough rotational modulation (from Table 2). The simulation runs are shown as line segments, with the lower points for 6010 Å and the higher ones for 3870 Å; for run  $\mathcal{M}(\mathcal{A} = 10)^+$  the maximum transit residuals expected from Figure 9 are added as asterisks connected by a dashed line segment. The stars for which both rotational modulation and transit residuals are shown in Table 1 are shown by name, roughly centered on the values in the table, moved slightly to reduce overlap where needed.

as a more extended and less dark feature. Interestingly, such tendencies were reported for the well-observed stars CoRoT-2 and Kepler-17 from exoplanet transit modeling, as discussed in Sect. 2.

Rotation-modulation analyses and Doppler-imaging studies may suggest large spotted areas, but the limited angular resolution of these methods does not provide unambiguous information about any finer-scale structuring within such spotted areas. The transit light-curve analyses of CoRoT-2 and Kepler-17 discussed in Sect. 2 is certainly suggestive of the existence of smaller starspots than inferred from rotation modulation or Doppler imaging, and of larger areas having smaller filling factors, causing larger spotted areas to appear brighter.

Evidence for a population of smaller and rather uniformly distributed population of starspots in cool stars was also inferred from observations of members of the Pleiades cluster, a group of  $\sim 125$  Myr-old and thus quite active cool stars: Guo *et al.* (2018) point out that the characteristic photometric rotational modulation is typically substantially smaller than expected for a starspot coverage fraction deduced from TiO absorption bands in the case of stars covered by only few large spots, but that these observations can be reconciled if there are many smaller starspots that are more uniformly dis-

tributed about the stars in longitude. Similar evidence, albeit for an analysis based on mostly M-type stars, that very active stars may be covered by multitudes of relatively small spots rather than by a small number of larger ones also comes from their rather weak rotational modulation, as discussed by Jackson and Jeffries (2013).

A question for which the answer remains simply to be determined is whether the field dispersing from large active regions in a photosphere much more magnetically active than the Sun’s carries a population of pores and small spots: on the Sun, the network formed by decaying active regions is simply too weak to carry magnetic concentrations of the required magnitude. Consequently, we do not know from observations whether or not network concentrations on a much more active star would form or maintain dark pores and small spots, or whether sufficiently strong regions would function as nest sites for newly emerging regions. Magnetoconvective experiments, however, do support the possibility of spontaneous formation, other than upon flux emergence, of at least pores in settings with a sufficiently high mean magnetic flux density (*e.g.*, Kitiashvili *et al.* 2010).

Another issue that needs attention in both modeling and observations is that of extremely large bipoles. If one takes the characteristic rate of flux emergence of active regions (see Sect. 3.1), then the emergence of very large regions should take many weeks to several months. This makes them appear as persistent longitudes of activity in rotational modulation curves. This is not inconsistent with observed stellar signals, but one certainly needs to question how to better constrain the properties of extremely large regions that are rarely or never observed on the Sun.

Zaleski *et al.* (2019) model transit residuals of Kepler-71 allowing for dark spot regions as well as bright facular regions. They conclude that the facular patches have a brightness contrast of  $1.1 \times -1.25 \times$  the quiet photosphere. Such values would be expected for areas with characteristic magnetic flux densities of 100 G or more. Extended such facular areas do occur in model  $\mathcal{M}(\mathcal{A} = 30)^+$ , but pores and spots within them limit the limb brightening to less than what appears to exist on Kepler-71. The interpretation of the relatively bright limb facular regions on the late G-type Kepler-71 is beyond the scope of this study.

## 7. CONCLUSIONS

In summary, regarding the results from the present flux-transport model in comparison with observations:

The flux-dispersal model based on solar empirical properties appears consistent with stellar observations of rotational modulation and transit residuals for Jupiter-

class exoplanets, particularly when the infrequent formation of large active regions with fluxes of a few times  $10^{23}$  Mx (or somewhat more) is allowed for.

An extrapolation of the power-law spectrum of solar active-region sizes to regions with corresponding fluxes of  $3 \times 10^{23}$  Mx yields results consistent with, although possibly somewhat below, observed rotational modulation and transit residuals. Such infrequent large regions would contain sufficient energy to power superflares that are detected with low occurrence frequencies on moderately to very active cool stars.

The surface flux-transport model is quantitatively consistent with a shift from facula-dominated to spot-dominated brightness changes with activity, as observed for cool stars.

For moderately to very active Sun-like stars, the model predicts large area filling factors for bright faculae and dark pores and spots, such that transits of stars substantially more active than the Sun will rarely, if ever, cross over sizable patches of truly quiet-star photosphere. Consequently, limb-darkening curves derived from observed transits of active stars are not directly comparable to convective-atmosphere models that do not incorporate magnetoconvective effects associated with regions of high magnetic flux density. For studies that involve passbands or spectral lines with significant chromospheric contributions, one should expect nearly ubiquitous spectral contamination of transit spectra by stellar features.

Facular contributions result in a wavelength-dependent change in the observed limb darkening that elevates the spectrum increasingly toward shorter wavelengths relative to a nonmagnetic spectrum, thus mimicking a bluer or hotter photosphere. Limb-darkening curves derived by using minima of a series of transits on active stars will be contaminated by faculae and spots, and should be used with caution if assumed characteristic for the average quiet stellar photosphere. Using the minima in residuals of a series of transits as the reference from which residuals are computed causes facular contributions to be underestimated and the inferred limb-darkening curves to be in error.

The model results raise the possibility that large starspots inferred from spot modeling are in fact clusters of smaller spots. This is consistent with the size-brightness correlation seen in analyses of several dozen transits of the active stars CoRoT-2 and Kepler-17.

The compatibility of the model results with observations is encouraging. On the one hand, it suggests that the solar paradigm may hold at least for early G-type stars of moderately high activity, and that this can thus be used to learn more about stellar magnetic activity

and transit spectroscopy of exoplanetary atmospheres alike. On the other hand, the multitude of parameters going into the model (many of which are discussed in Sect. 3.1) require testing by large-scale magnetoconvective modeling and empirical verification, while also quiet-star limb-darkening curves need to be established and validated. In order to expand this study to cooler stars, of which many more are available than are truly Sun-like stars, more information needs to be obtained on how to implement a surface-flux transport model at different spectral types and rotation rates (including the many unknowns listed at the beginning of Sect. 2).

This work reinforces the importance of studying stellar surface activity not only for its own sake, but also for the application of exoplanet transit spectroscopy: differences in inferred wavelength-dependent radii of a few hundred to a few thousand kilometers, increasing with

activity, should be anticipated as a result of stellar surface features for stars of moderately high activity and Jupiter-class exoplanets.

#### ACKNOWLEDGMENTS

This work was made possible by the support of the International Space Science Institute in Bern, CH. I am also grateful for the support of the US National Solar Observatory, and I thank Adam Kowalski there, Ben Rackham at MIT, Mark Cheung at LMSAL, Jeffrey Linsky at JILA, and an anonymous referee for helpful comments and for suggestions to improve the presentation. This research has made use of the SIMBAD database, operated at CDS, Strasbourg, France.

#### REFERENCES

- Aulanier, G., Démoulin, P., Schrijver, C. J., Janvier, M., Pariat, E., & Schmieder, B.: 2013, *A&A* 549, A66
- Bakos, G. Á., Hartman, J., Torres, G., Latham, D. W., Kovács, Géza, Noyes, R. W., Fischer, D. A., Johnson, J. A., Marcy, G. W., Howard, A. W., Kipping, D., Esquerdo, G. A., Shporer, A., Béky, B., Buchhave, L. A., Perumpilly, G., Everett, M., Sasselov, D. D., Stefanik, R. P., Lázár, J., Papp, I., & Sári, P.: 2011, *ApJ* 742(2), 116
- Barkaoui, K., Burdanov, A., Hellier, C., Gillon, M., Smalley, B., Maxted, P. F. L., Lendl, M., Triaud, A. H. M. J., Anderson, D. R., McCormac, J., Jehin, E., Almléaky, Y., Armstrong, D. J., Benkhaldoun, Z., Bouchy, F., Brown, D. J. A., Cameron, A. C., Daassou, A., Delrez, L., Ducrot, E., Foxell, E., Murray, C., Nielsen, L. D., Pepe, F., Pollacco, D., Pozuelos, F. J., Queloz, D., Segransan, D., Udry, S., Thompson, S., & West, R. G.: 2019, *AJ* 157(2), 43
- Beeck, B., Schüssler, M., Cameron, R. H., & Reiners, A.: 2015a, *A&A* 1581, A42
- Beeck, B., Schüssler, M., Cameron, R. H., & Reiners, A.: 2015b, *A&A* 581, A43
- Berdugina, S. V.: 2005, *Living Reviews in Solar Physics* 2, 8
- Bradshaw, S. J. & Hartigan, P.: 2014, *ApJ* 795(1), 79
- Brouwer, M. P. & Zwaan, C.: 1990, *Solar Phys.* 129, 221
- Brown, T. M.: 2001, *ApJ* 553(2), 1006
- Brun, A. S. & Browning, M. K.: 2017, *Living Reviews in Solar Physics* 14(1), 4
- Bruno, Giovanni, Lewis, Nikole K., Alam, Munazza K., López-Morales, Mercedes, Barstow, Joanna K., Wakeford, Hannah R., Sing, David K., Henry, Gregory W., Ballester, Gilda E., Bourrier, Vincent, Buchhave, Lars A., Cohen, Ofer, Mikal-Evans, Thomas, García Muñoz, Antonio, Lavvas, Panayotis, & Sanz-Forcada, Jorge: 2020, *MNRAS* 491(4), 5361
- Cauley, P. W., Kuckein, C., Redfield, S., Shkolnik, E. L., Denker, C., Llama, J., & M, Verma: 2018, *AJ* 156, 189
- Cuntz, M., Saar, S. H., & Musielak, Z. E.: 2000, *ApJL* 533(2), L151
- David, T. J., Cody, A. M., Hedges, C. L., Mamajek, E. E., Hillenbrand, L. A., Ciardi, D. R., Beichman, C. A., Petigura, E. A., Fulton, B. J., Isaacson, H. T., Howard, A. W., Gagné, J., Saunders, N. K., Rebull, L. M., Stauffer, J. R., Vasisht, G., & Hinkley, S.: 2019, *AJ* 158(2), 79
- Dravins, D., Ludwig, H.-G., Dahlén, E., & Pazira, H.: 2017, *A&A* 605, A90
- Espinoza, N. & Jordán, A.: 2015, *MNRAS* 450(2), 1879
- Fligge, M., Solanki, S. K., Pap, J. M., Fröhlich, C., & Wehrli, C.: 2001, *Journal of Atmospheric and Solar-Terrestrial Physics* 63(14), 1479
- Fligge, M., Solanki, S. K., Unruh, Y. C., Froehlich, C., & Wehrli, Ch.: 1998, *A&A* 335, 709
- Fröhlich, C.: 2016, *Journal of Space Weather and Space Climate* 6, A18
- Gibb, G. P. S., Mackay, D. H., Jardine, M. M., & Yeates, A. R.: 2016, *MNRAS* 456(4), 3624
- Guo, Z., Gully-Santiago, M., & Herczeg, G. J.: 2018, *ApJ* 868(2), 143

- Harvey, K. L. & Zwaan, C.: 1993, *Solar Phys.* 148(1), 85
- Hébrard, G., Collier Cameron, A., Brown, D. J. A., Díaz, R. F., Faedi, F., Smalley, B., Anderson, D. R., Armstrong, D., Barros, S. C. C., Bento, J., Bouchy, F., Doyle, A. P., Enoch, B., Gómez Maqueo Chew, Y., Hébrard, É. M., Hellier, C., Lendl, M., Lister, T. A., Maxted, P. F. L., McCormac, J., Moutou, C., Pollacco, D., Queloz, D., Santerne, A., Skillen, I., Southworth, J., Tregloan-Reed, J., Triaud, A. H. M. J., Udry, S., Vanhuyse, M., Watson, C. A., West, R. G., & Wheatley, P. J.: 2013, *A&A*549, A134
- Herrero, E., Ribas, I., Jordi, C., Morales, J. C., Perger, M., & Rosich, A.: 2016, *A&A*586, A131
- Jackson, R. J. & Jeffries, R. D.: 2013, *MNRAS*431(2), 1883
- Kitiashvili, I. N., Kosovichev, A. G., Wray, A. A., & Mansour, N. N.: 2010, *ApJ*719(1), 307
- Komm, R. W., Howard, R. F., & Harvey, J. W.: 1993, *Solar Phys.* 147, 207
- Kopp, G.: 2016, *Journal of Space Weather and Space Climate* 6, A30
- Koppenhoefer, J., Saglia, R. P., Fossati, L., Lyubchik, Y., Mugrauer, M., Bender, R., Lee, C. H., Riffeser, A., Afonso, P., Greiner, J., Henning, Th., Neuhäuser, R., Snellen, I. A. G., Pavlenko, Y., Verdugo, M., & Vogt, N.: 2013, *MNRAS* 435(4), 3133
- Kowalski, A., Schrijver, K., Pillet, V., & Criscuoli, S.: 2019, *Bull. Am. Astron. Soc.* 51(3), 149
- Lanza, A. F., Bonomo, A. S., & Rodonò, M.: 2007, *A&A*464(2), 741
- Lanza, A. F., Netto, Y., Bonomo, A. S., Parviainen, H., Valio, A., & Aigrain, S.: 2019, *A&A*626, A38
- Lanza, A. F., Pagano, I., Leto, G., Messina, S., Aigrain, S., Alonso, R., Auvergne, M., Baglin, A., Barge, P., Bonomo, A. S., Boumier, P., Collier Cameron, A., Comparato, M., Cutispoto, G., de Medeiros, J. R., Foing, B., Kaiser, A., Moutou, C., Parihar, P. S., Silva-Valio, A., & Weiss, W. W.: 2009, *A&A* 493(1), 193
- Lecavelier des Etangs, A., Hébrard, G., Blandin, S., Cassier, J., Deeg, H. J., Bonomo, A. S., Bouchy, F., Désert, J. M., Ehrenreich, D., Deleuil, M., Díaz, R. F., Moutou, C., & Vidal-Madjar, A.: 2017, *A&A* 603, A115
- Lee, J. N., Cahalan, R. F., & Wu, D. L.: 2016, *Journal of Space Weather and Space Climate* 6, A33
- Lehmann, L. T., Hussain, G. A. J., Jardine, M. M., Mackay, D. H., & Vidotto, A. A.: 2019, *MNRAS*483(4), 5246
- Linsky, J. L.: 2019, *Host Stars and their Effects on Exoplanet Atmospheres*, Vol. 955, Springer, Lecture Notes in Physics Vol. 955
- Linsky, J. L., Bushinsky, R., Ayres, T., Fontenla, J., & France, K.: 2012, *ApJ*745(1), 25
- Lockwood, G. W., Skiff, B. A., & Radick, R. R.: 1997, *ApJ.* 485, 789
- Maehara, H., Shibayama, T., Notsu, S., Notsu, Y., Nagao, T., Kusaba, S., Honda, S., Nogami, D., & Shibata, K.: 2012, *Nature* 485, 478
- Mancini, L., Kemmer, J., Southworth, J., Bott, K., Mollière, P., Ciceri, S., Chen, G., & Henning, Th.: 2016, *MNRAS* 459(2), 1393
- Martinez Pillet, V., Moreno-Insertis, F., & Vazquez, M.: 1993, *A&A*274, 521
- Mittag, M., Schmitt, J. H. M. M., & Schröder, K. P.: 2018, *A&A*618, A48
- Montet, Benjamin T., Tovar, Guadalupe, & Foreman-Mackey, Daniel: 2017, *ApJ*851(2), 116
- Murgas, F., Chen, G., Pallé, E., Nortmann, L., & Nowak, G.: 2019, *A&A*622, A172
- Neckel, H. & Labs, D.: 1994, *Solar Phys.* 153(1-2), 91
- Nikolov, N., Sing, D. K., Burrows, A. S., Fortney, J. J., Henry, G. W., Pont, F., Ballester, G. E., Aigrain, S., Wilson, P. A., Huitson, C. M., Gibson, N. P., Désert, J. M., Lecavelier Des Etangs, A., Showman, A. P., Vidal-Madjar, A., Wakeford, H. R., & Zahnle, K.: 2015, *MNRAS*447(1), 463
- Norris, C. M., Beeck, B., Unruh, Y. C., Solanki, S. K., Krivova, N. A., & Yeo, K. L.: 2017, *A&A* 605, A45
- Notsu, Y., Honda, S., Maehara, H., Notsu, S., Namekata, K., Nogami, D., & Shibata, K.: 2017, *PASJ* 69(1), 12
- Notsu, Y., Honda, S., Maehara, H., Notsu, S., Shibayama, T., Nogami, D., & Shibata, K.: 2015, *PASJ* 67(3), 33
- Notsu, Y., Shibayama, T., Maehara, H., Notsu, S., Nagao, T., Honda, S., Ishii, T. T., Nogami, D., & Shibata, K.: 2013, *ApJ.* 771, 127
- Noyes, R. W., Hartmann, L. W., Baliunas, S. L., Duncan, D. K., & Vaughan, A. H.: 1984, *ApJ*279, 763
- Oshagh, M., Santos, N. C., Ehrenreich, D., Haghhighipour, N., Figueira, P., Santerne, A., & Montalto, M.: 2014, *A&A*568, A99
- Patten, B. M. & Simon, Th.: 1996, *ApJSS* 106, 489
- Pinhas, A., Rackham, B. V., Madhusudhan, N., & Apai, D.: 2018, *MNRAS* 480, 5314
- Pont, F., Knutson, H., Gilliland, R. L., Moutou, C., & Charbonneau, D.: 2008, *MNRAS*385(1), 109

- Rackham, B., Pinhas, A., Apai, D., Haywood, R., Cegla, H., Espinoza, N., Teske, J., Gully-Santiago, M., Rau, G., Morris, B. M., Angerhausen, D., Barclay, Th., Carone, L., Cauley, P. W., de Wit, J., Domagal-Goldman, S., Dong, C., Dragomir, D., Giampapa, M. S., Hasegawa, Y., Hinkel, N. R., Hu, R., Jordán, A., Kitiashvili, I., Kreidberg, L., Lisse, C., Llama, J., López-Morales, M., Mennesson, B., Molaverdikhani, K., Osip, D. J., & Quintana, E. V.: 2019a, *Bull. Am. Astron. Soc.* 51(3), 328
- Rackham, B. V., Apai, D., & Giampapa, M. S.: 2018, *ApJ* 853(2), 122
- Rackham, B. V., Apai, D., & Giampapa, M. S.: 2019b, *AJ* 157(3), 96
- Radick, R. R., Lockwood, G. W., Henry, G. W., Hall, J. C., & Pevtsov, A. A.: 2018, *ApJ* 855(2), 75
- Reiners, A.: 2012, *Living Reviews in Solar Physics* 9(1), 1
- Schrijver, C. J.: 2001, *ApJ* 547, 475
- Schrijver, C. J., Beer, J., Baltensperger, U., Cliver, E. W., Güdel, M., Hudson, H. S., McCracken, K. G., Osten, R. A., Peter, T., Soderblom, D. R., Usoskin, I. G., & Wolff, E. W.: 2012, *Journal of Geophysical Research (Space Physics)* 117, 8103
- Schrijver, C. J. & DeRosa, M. L.: 2003, *Solar Phys.* 212, 165
- Schrijver, C. J., DeRosa, M. L., & Title, A. M.: 2002, *ApJ* 577, 1006
- Schrijver, C. J., DeRosa, M. L., & Title, A. M.: 2003, *ApJ* 590, 493
- Schrijver, C. J. & Harvey, K. L.: 1994, *Solar Phys.* 150, 1
- Schrijver, C. J. & Liu, Y.: 2008, *Solar Phys.* 252, 19
- Schrijver, C. J. & Title, A. M.: 2001, *ApJ* 551, 1099
- Schrijver, C. J. & Title, A. M.: 2005, *ApJ* 619, 1077
- Schrijver, C. J., Title, A. M., Van Ballegoijen, A. A., Hagenaar, H. J., & Shine, R. A.: 1997, *ApJ* 487, 424
- Schrijver, C. J. & Zwaan, C.: 2000, *Solar and Stellar Magnetic Activity*, Cambridge University Press, Cambridge, U.K.
- Seager, S. & Sasselov, D. D.: 2000, *ApJ* 537(2), 916
- See, V., Matt, S. P., Folsom, C. P., Boro Saikia, S., Donati, J.-F., Fares, R., Finley, A. J., Hébrard, É. M., Jardine, M. M., Jeffers, S. V., Lehmann, L. T., Marsden, S. C., Mengel, M. W., Morin, J., Petit, P., Vidotto, A. A., Waite, I. A., & The BCool Collaboration: 2019, *ApJ* 876(2), 118
- Shapiro, A. I., Solanki, S. K., Krivova, N. A., Schmutz, W. K., Ball, W. T., Knaack, R., Rozanov, E. V., & Unruh, Y. C.: 2014, *A&A* 569, A38
- Shibayama, T., Maehara, H., Notsu, S., Notsu, Y., Nagao, T., Honda, S., Ishii, T. T., Nogami, D., & Shibata, K.: 2013, *ApJSS* 209, 5
- Silva-Valio, A. & Lanza, A. F.: 2011, *A&A* 529, A36
- Sing, D. K., Pont, F., Aigrain, S., Charbonneau, D., Désert, J. M., Gibson, N., Gilliland, R., Hayek, W., Henry, G., Knutson, H., Lecavelier Des Etangs, A., Mazeh, T., & Shporer, A.: 2011, *MNRAS* 416(2), 1443
- Solanki, S. K. & Schmidt, H. U.: 1993, *A&A* 267(1), 287
- Solanki, S. K. & Unruh, Y. C.: 2004, *MNRAS* 348(1), 307
- Strassmeier, K. G.: 2009, *A&A Rv* 17(3), 251
- Taylor, P. O.: 1989, *Journal of the American Association of Variable Star Observers (JAAVSO)* 18, 65
- Tregloan-Reed, Jeremy, Southworth, John, Burgdorf, M., Novati, S. Calchi, Dominik, M., Finet, F., Jørgensen, U. G., Maier, G., Mancini, L., Prof, S., Ricci, D., Snodgrass, C., Bozza, V., Browne, P., Dodds, P., Gerner, T., Harpsøe, K., Hinse, T. C., Hundertmark, M., Kains, N., Kerins, E., Liebig, C., Penny, M. T., Rahvar, S., Sahu, K., Scarpetta, G., Schäfer, S., Schönebeck, F., Skottfelt, J., & Surdej, J.: 2015, *MNRAS* 450(2), 1760
- Unruh, Y. C., Krivova, N. A., Solanki, S. K., Harder, J. W., & Kopp, G.: 2008, *A&A* 486(1), 311
- Valio, A., Estrela, R., Netto, Y., Bravo, J. P., & de Medeiros, J. R.: 2017, *ApJ* 835(2), 294
- Van Ballegoijen, A. A., Cartledge, N. P., & Priest, E. R.: 1998, *ApJ* 501, 866
- Vidotto, A. A., Gregory, S. G., Jardine, M., Donati, J. F., Petit, P., Morin, J., Folsom, C. P., Bouvier, J., Cameron, A. C., Hussain, G., Marsden, S., Waite, I. A., Fares, R., Jeffers, S., & do Nascimento, J. D.: 2014, *MNRAS* 441(3), 2361
- Yeo, K. L., Solanki, S. K., Norris, C. M., Beeck, B., Unruh, Y. C., & Krivova, N. A.: 2017, *PhRvL* 119, 9.1102
- Zaleski, S. M., Valio, A., Marsden, S. C., & Carter, B. D.: 2019, *MNRAS* 484(1), 618
- Zhang, J., Wang, Y., & Liu, Y.: 2010, *ApJ* 723, 1006